

# The X-SERVS survey: new *XMM-Newton* point-source catalog for the XMM-LSS field

C.-T.J. Chen<sup>1,2\*</sup>, W.N. Brandt<sup>1,2,3</sup>, B. Luo<sup>4</sup>, P. Ranalli<sup>5</sup>, G. Yang<sup>1,2</sup>, F.E. Bauer<sup>6,7,8</sup>, D.D. Kelson<sup>9</sup>, M. Lacy<sup>10</sup>, K. Nyland<sup>10</sup>, P. Tozzi<sup>11</sup>, F. Vito<sup>1,2</sup>, M.J. Jarvis<sup>13,14</sup>, B.D. Lehmer<sup>15</sup>, D.P. Schneider<sup>1,2</sup>, O. Shemmer<sup>16</sup>, I. Smail<sup>17</sup>, M. Vaccari<sup>14,18</sup>, C. Vignali<sup>19,20</sup>, Y.Q. Xue<sup>21,22</sup>, M. Tanaka<sup>23</sup>, D.M. Alexander<sup>17</sup>, K.E. Chow<sup>24</sup>, B. Häußler<sup>25</sup>, M. Paolillo<sup>26</sup>, J.D. Silverman<sup>27</sup>, and J.R. Trump<sup>28</sup>

<sup>1</sup>Department of Astronomy & Astrophysics, 525 Davey Lab, The Pennsylvania State University, University Park, PA 16802, USA

<sup>2</sup>Institute for Gravitation and the Cosmos, The Pennsylvania State University, University Park, PA 16802, USA

<sup>3</sup>Department of Physics, The Pennsylvania State University, University Park, PA 16802, USA

<sup>4</sup>School of Astronomy and Space Science, Nanjing University, Nanjing 210093, China

<sup>5</sup>Lund Observatory, Box 43, 22100 Lund, Sweden

<sup>6</sup>Instituto de Astrofísica and Centro de Astroingeniería, Facultad de Física, Pontificia Universidad Católica de Chile, Casilla 306, Santiago 22, Chile

<sup>7</sup>Millennium Institute of Astrophysics (MAS), Chile

<sup>8</sup>Space Science Institute, 4750 Walnut Street, Suite 205, Boulder, Colorado 80301, USA

<sup>9</sup>The Observatories, The Carnegie Institution for Science, 813 Santa Barbara St., Pasadena, CA 91101

<sup>10</sup>National Radio Astronomy Observatory, 520 Edgemont Road, Charlottesville, VA 22903, USA

<sup>11</sup>INAF, Osservatorio Astrofisico di Arcetri, Largo E. Fermi 5, I-50125, Firenze, Italy

<sup>13</sup>Oxford Astrophysics, Denys Wilkinson Building, University of Oxford, Keble Road, Oxford OX1 3RH, UK

<sup>14</sup>Department of Physics, University of the Western Cape, Bellville 7535, South Africa

<sup>15</sup>Department of Physics, University of Arkansas, 226 Physics Building, 825 West Dickson Street, Fayetteville, AR 72701, USA

<sup>16</sup>Department of Physics, University of North Texas, Denton, TX 76203, USA

<sup>17</sup>Centre for Extragalactic Astronomy, Department of Physics, Durham University, South Road, Durham, DH1 3LE, UK

<sup>18</sup>INAF – Istituto di Radioastronomia, via Gobetti 101, 40129 Bologna, Italy

<sup>19</sup>Dipartimento di Fisica e Astronomia, Università degli Studi di Bologna, Via Gobetti 93/2, 40129 Bologna, Italy

<sup>20</sup>INAF – Osservatorio Astronomico di Bologna, Via Gobetti 93/3, 40129 Bologna, Italy

<sup>21</sup>CAS Key Laboratory for Research in Galaxies and Cosmology, Department of Astronomy, University of Science and Technology of China, Hefei 230026, China

<sup>22</sup>School of Astronomy and Space Science, University of Science and Technology of China, Hefei 230026, China

<sup>23</sup>National Astronomical Observatory of Japan, 2-21-1 Osawa, Mitaka, Tokyo 181-8588, Japan

<sup>24</sup>CSIRO Astronomy and Space Science, PO Box 76, Epping, NSW, 1710, Australia

<sup>25</sup>European Southern Observatory, Alonso de Cordova 3107, Vitacura, Santiago, Chile

<sup>26</sup>Dip.di Fisica Ettore Pancini, Università di Napoli Federico II, via Cintia, 80126, Napoli, Italy

<sup>27</sup>Kavli Institute for the Physics and Mathematics of the Universe, The University of Tokyo, Kashiwa, Japan 277-8583 (Kavli IPMU, WPI)

<sup>28</sup>Department of Physics, University of Connecticut, 2152 Hillside Road, Storrs, CT 06269, USA

Accepted XXX. Received YYY; in original form ZZZ

**Key words:** catalogues – surveys – galaxies:active – X-rays:galaxies – quasars: general

## 1 INTRODUCTION

Due to the penetrating nature of X-ray emission and its ubiquity from accreting supermassive black holes (SMBHs), extragalactic X-ray surveys have provided an effective census of active galactic nuclei (AGNs), including obscured systems, in the distant universe. Over at least the past three decades, the overall design of cosmic X-ray surveys has fol-

lowed a “wedding cake” strategy. At the extremes of this strategy, some surveys have ultra-deep X-ray coverage and a narrow “pencil-beam” survey area ( $\lesssim 1 \text{ deg}^2$ ), while others have shallow X-ray coverage over a wide survey area ( $\approx 10\text{--}10^4 \text{ deg}^2$ ). The wealth of data from cosmic X-ray surveys (and their co-located multiwavelength surveys) have provided a primary source of information in shaping understanding of how SMBHs grow through cosmic time, where deep surveys generally sample high-redshift, moderately luminous AGNs, and wide-field surveys generally probe the

\* E-mail: ctchen@psu.edu

**Table 1.** Current and scheduled 1–10 deg<sup>2</sup> multiwavelength coverage of the X-SERVS fields. References: [a] Franzen et al. (2015); [b] Jarvis et al. (2017); [c] Oliver et al. (2012); [d] Lonsdale et al. (2003); [e] Mauduit et al. (2012). Note that SERVS has recently been expanded to cover the full LSST deep drilling fields (*Spitzer* Program ID 11086). [f] Jarvis et al. (2012); [g] [http://www.ast.cam.ac.uk/~mbanerji/VEILS/veils\\_index.html](http://www.ast.cam.ac.uk/~mbanerji/VEILS/veils_index.html); [h] Diehl et al. (2014); [i] Aihara et al. (2017); [j] Tonry et al. (2011); [k] Vaccari et al. (2016); [l] <http://www.lsst.org/News/enews/deep-drilling-201202.html>; [m] Kelson et al. (2014); Patel et al. (2015); [n] Coil et al. (2010); [o] <https://devilsurvey.org/wp/>; [p] <http://www.roe.ac.uk/~ciras/MOONS/VLT-MOONS.html>; [q] <http://www.galex.caltech.edu/researcher/techdoc-ch2.html>.

Band	Survey Name	Coverage (XMM-LSS, W-CDF-S, ELAIS-S1); Notes
Radio	Australia Telescope Large Area Survey ( <b>ATLAS</b> ) <sup>a</sup> <b>MIGHTEE</b> Survey (Starting Soon) <sup>b</sup>	–, 3.7, 2.7 deg <sup>2</sup> ; 15 μJy rms depth at 1.4 GHz 4.5, 3, 4.5 deg <sup>2</sup> ; 1 μJy rms depth at 1.4 GHz
FIR	<i>Herschel</i> Multi-tiered Extragal. Surv. ( <b>HerMES</b> ) <sup>c</sup>	0.6–18 deg <sup>2</sup> ; 5–60 mJy depth at 100–500 μm
MIR	<i>Spitzer</i> Wide-area IR Extragal. Survey ( <b>SWIRE</b> ) <sup>d</sup>	9.4, 8.2, 7.0 deg <sup>2</sup> ; 0.04–30 mJy depth at 3.6–160 μm
NIR	<i>Spitzer</i> Extragal. Rep. Vol. Survey ( <b>SERVS</b> ) <sup>e</sup> VISTA Deep Extragal. Obs. Survey ( <b>VIDEO</b> ) <sup>f</sup> VISTA Extragal. Infr. Legacy Survey ( <b>VEILS</b> ) <sup>g</sup>	4.5, 3, 4.5 deg <sup>2</sup> ; 2 μJy depth at 3.6 and 4.5 μm 4.5, 3, 4.5 deg <sup>2</sup> ; ZYJK <sub>s</sub> to $m_{AB} \approx 23.8\text{--}25.7$ 3, 3, 3 deg <sup>2</sup> ; JK <sub>s</sub> to $m_{AB} \approx 24.5\text{--}25.5$
Optical Photometry	Dark Energy Survey ( <b>DES</b> ) <sup>h</sup> Hyper Suprime-Cam ( <b>HSC</b> ) Deep Survey <sup>i</sup> Pan-STARRS1 Medium-Deep Survey ( <b>PS1MD</b> ) <sup>j</sup> VST Opt. Imaging of CDF-S and ES1 ( <b>VOICE</b> ) <sup>k</sup> SWIRE optical imaging <sup>d</sup> <b>LSST</b> deep-drilling field (Planned) <sup>l</sup>	9, 6, 9 deg <sup>2</sup> ; Multi-epoch griz, $m_{AB} \approx 27$ co-added 5.3, –, – deg <sup>2</sup> ; grizy to $m_{AB} \approx 25.3\text{--}27.5$ 8, –, 8 deg <sup>2</sup> ; Multi-epoch grizy, $m_{AB} \approx 26$ co-added –, 4.5, 3 deg <sup>2</sup> ; Multi-epoch ugri, $m_{AB} \approx 26$ co-added 8, 7, 6 deg <sup>2</sup> ; u'g'r'i'z' to $m_{AB} \approx 24\text{--}26$ 10, 10, 10 deg <sup>2</sup> ; ugrizy, $\gtrsim 10000$ visits per field
Optical/NIR Spectroscopy	Carnegie- <i>Spitzer</i> -IMACS Survey ( <b>CSI</b> ) <sup>m</sup> PRISM Multi-object Survey ( <b>PRIMUS</b> ) <sup>n</sup> AAT Deep Extragal. Legacy Survey ( <b>DEVILS</b> ) <sup>o</sup> VLT <b>MOONS</b> Survey (Scheduled) <sup>p</sup>	6.9, 4.8, 3.6 deg <sup>2</sup> ; 140000 redshifts, 3.6 μm selected 2.9, 2.0, 0.9 deg <sup>2</sup> ; 77000 redshifts to $i_{AB} \approx 23.5$ 3.0, 1.5, – deg <sup>2</sup> ; 43500 redshifts to $Y = 21.2$ 4.5, 3, 4.5 deg <sup>2</sup> ; 210000 redshifts to $H_{AB} \approx 23.5$
UV	<i>GALEX</i> Deep Imaging Survey <sup>q</sup>	8, 7, 7 deg <sup>2</sup> ; Depth $m_{AB} \approx 25$

high-luminosity, rare objects that are missed by surveys covering smaller volumes. However, narrow-field surveys lack the contiguous volume to encompass a wide range of cosmic large-scale structures, and wide-field surveys generally lack the X-ray sensitivity to track the bulk of the AGN population though the era of massive galaxy assembly (see Brandt & Alexander 2015 for a recent review).

Among extragalactic X-ray surveys, the medium-deep COSMOS survey over  $\approx 2$  deg<sup>2</sup> has the needed sensitivity-area combination to begin to track how a large fraction of distant SMBH growth relates to cosmic large-scale structures (e.g., Hasinger et al. 2007; Civano et al. 2016). However, even COSMOS cannot sample the full range of cosmic environments. The largest structures found in cold dark matter simulations are already as large as the angular extent of COSMOS at  $z \approx 1$  (80–100 Mpc in comoving size, which covers 2–3 deg<sup>2</sup>; e.g., see Klypin et al. 2016). Clustering analyses also demonstrate that COSMOS-sized fields are still subject to significant cosmic variance (e.g., Meneux et al. 2009; de la Torre et al. 2010; Skibba et al. 2014).

Therefore, to study SMBH growth across the full range of cosmic environments and minimize cosmic variance, it is necessary to obtain multiple medium-deep X-ray surveys in distinct sky regions (e.g., Driver & Robotham 2010; Moster et al. 2011) with multiwavelength data comparable to those

of COSMOS. In this work, we present a catalog of 5252 *XMM-Newton* sources detected over 5.3 deg<sup>2</sup> in one of the well-studied *Spitzer* Extragalactic Representative Volume Survey (SERVS, Mauduit et al. 2012) fields, the XMM-Large Scale Structure (XMM-LSS) region. This is the first field of the broader X-SERVS survey which aims to expand the parameter space of X-ray surveys with three  $> 3$  deg<sup>2</sup> surveys reaching COSMOS-like depth, including XMM-LSS, W-CDF-S, and ELAIS-S1. These three extragalactic fields have been chosen based on their excellent multiwavelength coverage and superior legacy value. We list the current and scheduled multiwavelength coverage of X-SERVS in Table 1.

The X-ray source catalog presented here has been generated using a total of 1.3 Ms of *XMM-Newton* AO-15 observations in the XMM-LSS field (specifically the region covered by SERVS), plus all archival *XMM-Newton* data in this same region. Our AO-15 observations target the central part of XMM-LSS adjacent to the Subaru *XMM-Newton* Deep Survey (SXDS, Ueda et al. 2008), transforming the complex archival *XMM-Newton* coverage in this region into a contiguous 5.3 deg<sup>2</sup> field with uniform X-ray coverage. The median exposure time with the PN instrument is  $\approx 46$  ks, reaching survey depths comparable to those of XMM-COSMOS (e.g., Cappelluti et al. 2009) and SXDS. We also present multiwavelength counterparts, basic photometric properties, and

spectroscopic redshifts obtained from the literature. Photometric redshifts are derived over a  $1 \text{ deg}^2$  region, demonstrating what will soon be possible over the entire  $5.3 \text{ deg}^2$  field. The excellent multiwavelength coverage in the X-SERVS XMM-LSS field will provide the necessary data for studying the general galaxy population and tracing large-scale structures. The combination of these multiwavelength data and the new X-ray source catalog (along with similar data for COSMOS and the other X-SERVS fields) will enable potent studies of SMBH growth across the full range of cosmic environments while minimizing cosmic variance effects.

This paper is organized as follows: in §2 we present the details of the new and archival observations, and the procedures for data reduction. In §3 we describe the X-ray source-searching strategies and the details of the production of the X-ray point-source catalog. §4 outlines the reliability assessment of the X-ray catalog using simulated X-ray observations. The survey sensitivity and the number counts are also presented here. In §5, we describe the multiwavelength identification methods and reliability assessments, as well as basic multiwavelength properties including spectroscopic and photometric redshifts. A summary is given in §6. The source catalog and the descriptions of columns are included in the Appendix §A. Throughout the paper, we assume a  $\Lambda\text{CDM}$  cosmology with  $H_0 = 70 \text{ km s}^{-1} \text{ Mpc}^{-1}$ ,  $\Omega_m = 0.3$ , and  $\Omega_\Lambda = 0.7$ . We adopt a Galactic column density  $N_{\text{H}} = 3.57 \times 10^{20} \text{ cm}^{-2}$  along the line of sight to the center of the source-detection region at RA =  $35.6625^\circ$ , DEC =  $-4.795^\circ$ . AB magnitudes are used unless noted otherwise.

## 2 XMM-NEWTON OBSERVATIONS IN THE XMM-LSS REGION AND DATA REDUCTION

### 2.1 XMM-Newton data in the XMM-LSS region

The XMM-LSS field has been targeted by a number of *XMM-Newton* surveys of different sensitivities (e.g., see Fig. 3 of Brandt & Alexander 2015 and Fig. 1 of Xue 2017). The original XMM-LSS survey was an  $\approx 11 \text{ deg}^2$  field typically covered by observations of  $\approx 10 \text{ ks}$  exposure time per pointing (Pacaud et al. 2006; Pierre et al. 2016). Within the  $11 \text{ deg}^2$  field,  $\approx 4 \text{ deg}^2$  were observed by the *XMM-Newton* Medium Deep Survey (XMDS,  $20 - 25 \text{ ks}$  exposure depth, Chiappetti et al. 2005). In addition, the Subaru *XMM-Newton* Deep Survey (SXDS, Ueda et al. 2008), adjacent to the XMDS field, covers a  $1.14 \text{ deg}^2$  area and reaches  $\approx 50 \text{ ks}$  exposure per pointing (Ueda et al. 2008). Moreover, the XMM-LSS field recently became a part of the  $25 \text{ deg}^2$  XMM-XXL-North field (Pierre et al. 2016), which has similar *XMM-Newton* coverage as the original XMM-LSS survey (i.e.,  $\approx 10 \text{ ks}$  depth).

In addition to the X-ray data, the XMM-LSS region has extensive multiwavelength coverage (see Table 1 for a summary). In particular, the central  $\approx 5 \text{ deg}^2$  area of the XMM-XXL-North field (i.e., the combination of the XMDS and SXDS fields) was selected to be one of the SERVS fields. This sky region is covered uniformly by multiple photometric and spectroscopic surveys (see Sec. 5 for more details), and is one of the deep drilling fields of the Dark Energy Survey (Diehl et al. 2014) and the upcoming Large Synoptic

Survey Telescope (LSST) surveys<sup>1</sup>. Compared to the relatively uniform multiwavelength data, archival *XMM-Newton* observations covering this sky region span a wide range of exposure time (see Table 2). In order to advance studies of accreting SMBHs and their environments, deep X-ray observations with similar areal coverage are required in addition to the rich multiwavelength data in this field. To this end, we obtained *XMM-Newton* AO-15 observations taken between July 2016 and February 2017 with a total of 1.3 Ms exposure time. Our AO-15 data include 67 *XMM-Newton* observations. In addition to the new data, we made use of all the overlapping archival *XMM-Newton* observations to create a sensitive *XMM-Newton* survey contiguously covering most of the SERVS data in the XMM-LSS region. After excluding observations that were completely lost due to flaring background (see §2.2), the archival data used here include 51 observations culled from the 10 ks XMM-LSS survey, 18 observations from XMDS with  $20 - 25 \text{ ks}$  exposures, four mosaic-mode observations<sup>2</sup> obtained as part of the XMM-XXL survey (Pierre et al. 2016), four archival *XMM-Newton* observations targeting galaxy clusters identified in the XMM-XXL-North and XMM-LSS surveys ( $\approx 30 - 100 \text{ ks}$ ), and the ten 50 ks observations from SXDS. We present the details of each observation in Table 2, and show the positions of each *XMM-Newton* observation used in this work in Fig. 1.

Our AO-15 observations were separated into two epochs to minimize the effects of background flaring. We first observed the XMM-LSS sky-region in the SERVS footprint with  $\approx 1 \text{ Ms}$  of *XMM-Newton* exposure time during July–August 2016. These first observations were screened for flaring backgrounds (§2.2); we then re-observed the background-contaminated sky regions using the remaining 0.3 Ms. We also observed the SXDS region in which one of the SXDS observations carried out in 2002 was severely affected by background flares. In this work, we present an X-ray source catalog obtained from a  $5.3 \text{ deg}^2$  sky-region with  $34.2^\circ \leq \alpha_{J2000} \leq 37.125^\circ$  and  $-5.72^\circ \leq \delta_{J2000} \leq -3.87^\circ$  (black rectangle in Fig 1). The sky region is primarily selected by the footprint of our AO-15 observations, with additional SXDS data within the SERVS footprint in the south-west corner. A total of 3.0 Ms of raw *XMM-Newton* observations are used for generating the X-ray source catalog.

### 2.2 Data preparation and background-flare filtering

We use the *XMM-Newton* Science Analysis System (SAS) 16.1.0<sup>3</sup> and HEASOFT 6.21<sup>4</sup> for our data analysis. The *XMM-Newton* Observation Data Files (ODFs) were processed with the SAS tasks EPICPROC (EPPROC and EMPROC for PN and MOS, respectively) to create MOS1, MOS2, PN, and PN out-of-time (OOT) event files for each ObsID. For

<sup>1</sup> <http://www.lsst.org/News/enews/deep-drilling-201202.html>.

<sup>2</sup> Each mosaic-mode observation is comprised of a number of 10 ks exposures, see [https://xmm-tools.cosmos.esa.int/external/xmm\\_user\\_support/documentation/uhb/mosaic.html](https://xmm-tools.cosmos.esa.int/external/xmm_user_support/documentation/uhb/mosaic.html).

<sup>3</sup> <https://www.cosmos.esa.int/web/xmm-newton/sas-release-notes-1610>.

<sup>4</sup> [https://heasarc.gsfc.nasa.gov/FTP/software/ftools/release/archive/Release\\_Notes\\_6.21](https://heasarc.gsfc.nasa.gov/FTP/software/ftools/release/archive/Release_Notes_6.21).

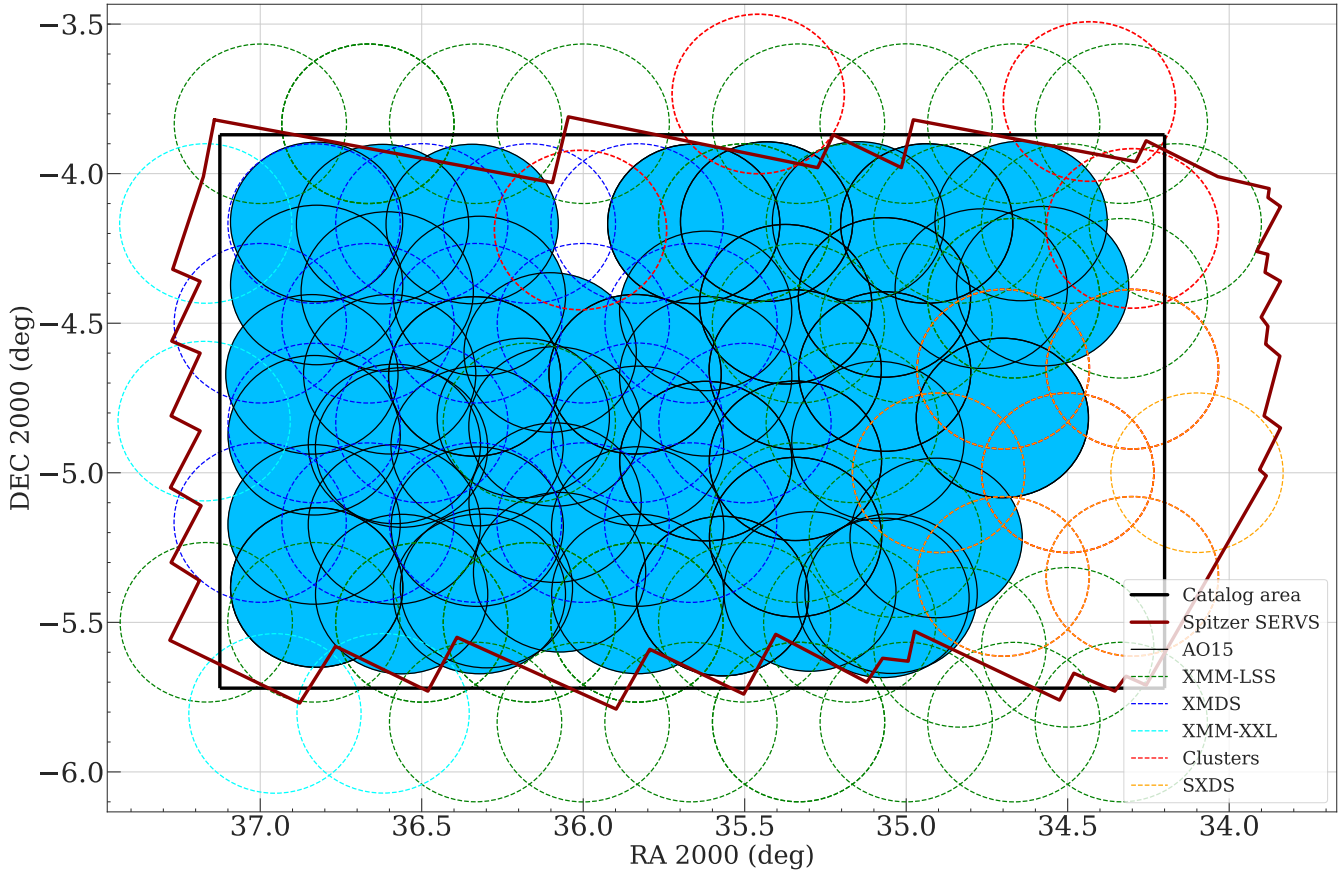


**Figure 1.** Locations of the *XMM-Newton* observations used in this work. The AO-15 observations are marked as the blue-filled circles with solid boundaries. The archival observations are marked as dashed circles. Circles with green, orange, blue, and cyan colors are for XMM-LSS, SXDS, XMDS, and XMM-XXL observations, respectively. The RA/DEC range of our catalog selection area is indicated by the black rectangle, and the *Spitzer* SERVS footprint is marked as the dark-red polygon. Our AO-15 observations do not cover the entirety of the SERVS region, because the existing data from SXDS (bottom-right corner, orange circles) and from deep X-ray cluster observations (top-middle and top-right, the red circles) reached the desired depth.

**Table 2.** The *XMM-Newton* data used to create the source catalog include 155 pointings with a total of 2.7 Ms of flare-filtered exposure time, of which 1.1 Ms is from the new AO-15 observations.<sup>a</sup> Columns from left to right: target field, *XMM-Newton* revolution, *XMM-Newton* ObsID, observation starting date/time, Right Ascension and Declination of the pointing center (J2000, degrees), cleaned exposure time for PN, MOS1, and MOS2 in each pointing. This table is available in its entirety online.

Field	Revolution	ObsID	Date (UT)	R.A.	Decl.	GTI (PN) (ks)	GTI (MOS1) (ks)	GTI (MOS2) (ks)
AO-15	3054	0780450101	2016-08-13T01:34:06	35.81072	-5.15989	20.91	23.61	23.61
XMM-LSS	1205	0404965101	2006-07-09T08:08:08	35.80953	-5.48532	3.44	10.36	9.91
XMDS	287	0111110401	2001-07-03T14:01:54	35.97582	-5.15253	21.40	27.20	27.40
SXDS	118	0112370101	2000-07-31T21:57:54	34.47819	-4.98115	39.13	42.70	42.83
XMM-XXL-N	2137	0677580101	2011-08-10T01:53:35	38.00217	-4.49993	4.94	5.93	5.52
XLSSJ022404.0-041328	0928	0210490101	2005-01-01T19:08:30	36.03267	-4.20230	80.28	87.98	87.98

<sup>a</sup>: MOS only (MOS1 and MOS2 have the same exposure time). For PN, the total flare-filtered time is 2.3 Ms, of which 0.9 Ms is from the new AO-15 observations.

observations taken in mosaic mode or with unexpected interruptions due to strong background flares, we use the SAS task EMOSAIC\_PREP to separate the event files into individual pseudo-exposures and assign pseudo-exposure IDs.<sup>5</sup> For

the mosaic-mode observations, we also determine the sky coordinates of each pseudo-exposure using the AHFRA and AHFDEC values in the attitude files created using the SAS task ATTHKGEN.

<sup>5</sup> For mosaic-mode observations, multiple exposures are stored in a single-event file for each EPIC camera after ODF processing. EMOSAIC\_PREP separates the single event file into multiple pseudo event files with the same ObsID but different EXP\_ID and EXPIDSTR values. EMOSAIC\_PREP assigns a separate EXP\_ID for each event file, which is necessary for SAS source-detection tasks.

the SAS tasks. For observations with unexpected interruptions, the exposure is separated into multiple event files with the same ObsID and EXP\_ID by EPICPROC, but with different EXPIDSTR values. EMOSAIC\_PREP assigns a separate EXP\_ID for each event file, which is necessary for SAS source-detection tasks.

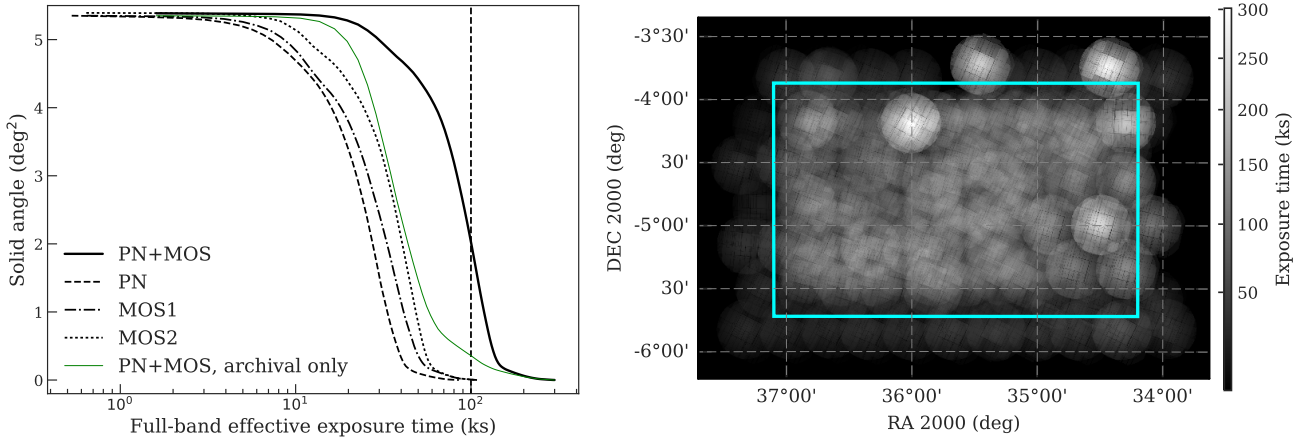


**Figure 2.** *Left* – The black solid line shows the cumulative survey solid angle as a function of full-band effective (i.e., vignetted) PN+MOS exposure for observations used in this work. Distributions for individual instruments are indicated as the dashed line (PN), dash-dotted line (MOS1), and dotted line (MOS2). For comparison, the cumulative survey solid angle for the archival *XMM-Newton* data is also shown as the thin green line. The dashed vertical line marks exposure time = 100 ks. *Right* – Full-band survey effective exposure map (PN + MOS). The 5.3 deg<sup>2</sup> survey region from which the X-ray source catalog is constructed is marked as the cyan rectangular box. Except for several regions with deep *XMM-Newton* follow-up observations of galaxy clusters, the *XMM-Newton* coverage in our survey region is generally uniform.

For each event file, we create single event light curves in time bins of 100 s for high (10–12 keV) and low (0.3–10 keV) energies using EVSELECT to search for time intervals without significant background flares (the “good time intervals”, GTIs). We first remove time intervals with 10–12 keV count rates exceeding  $3\sigma$  above the mean, and then repeat the  $3\sigma$  clipping procedure for the low-energy light curves. Since background flares usually manifest themselves as a high-count-rate tail in addition to the Gaussian-shape count-rate histogram, adopting the  $3\sigma$  clipping rule can effectively remove the high-count-rate tail while retaining useful scientific data. For a small number of event files with intense background flares, we filter the event files using the nominal count rate thresholds suggested by the *XMM-Newton* Science Operations Centre.<sup>6</sup> We exclude 12 pointings with  $\text{GTI} < 2 \text{ ks}$  from our analysis. A total of 2.7 Ms (2.3 Ms) of MOS (PN) exposure remains after flare filtering, including 1.1 Ms (0.9 Ms) from AO-15 and 1.6 Ms (1.4 Ms) from the archival data. After screening for background flares, we further exclude events in energy ranges that overlap with the instrumental background lines (Al K $\alpha$  lines at 1.45–1.54 keV for MOS and PN, which usually accounts for  $\approx 10\%$  of the mean counts<sup>7</sup>; Cu lines at 7.2–7.6 keV and 7.8–8.2 keV for PN, which accounts for 30% of the 2–10 keV counts<sup>8</sup>).

From the flare-filtered, instrumental-line-removed event files, we construct images with a 4'' pixel size using EVSELECT<sup>9</sup> in the following bands: 0.5–2 keV (soft) and 2–10 keV (hard), and 0.5–10 keV (full) bands. For each image, we gen-

erate exposure maps with and without vignetting corrections using the SAS task EEXPMAP. We set USEFASTPIXELIZATION=0 and ATTRIBIN=0.5 in order to obtain more accurate exposure maps. The exposure maps without vignetting-corrections are only used for generating background maps in §3. Detector masks were also generated using the SAS task EMASK. The distribution of exposure values across the XMM-LSS field and the PN+MOS1+MOS2 exposure map are presented in Fig. 2. The median PN exposure time of the full 5.3 deg<sup>2</sup> survey region is  $\approx 45.8$  ks. For the central  $\approx 4.5$  deg<sup>2</sup> region covered by SERVS, the median PN exposure time is 48.5 ks.

### 3 THE MAIN X-RAY SOURCE CATALOG

#### 3.1 First-pass source detection and astrometric correction

The astrometric accuracy of *XMM-Newton* observations can be affected by the pointing uncertainties of *XMM-Newton*. This uncertainty is usually smaller than a few arcsec, but can be as large as  $\approx 10''$  (e.g., Cappelluti et al. 2007; Watson et al. 2008; Rosen et al. 2016). To achieve better astrometric accuracy and to minimize any systematic offsets between different *XMM-Newton* observations, we run an initial pass of source detection for each observation and then use the first-pass source list to register the *XMM-Newton* observations onto a common WCS frame. The first-pass source detection methods are outlined below:

- (i) For the exposure taken by each of the three instruments for each observation, we generate a temporary source list using the SAS task EWAVELET with a low likelihood threshold (THRESHOLD=4). EWAVELET is a wavelet-based algorithm that runs on the count-rate image generated using the image and exposure map extracted as described in §2.2.
- (ii) We use the temporary source list as an input to generate background images using the SAS task ESPLINEMAP with

<sup>6</sup> <https://www.cosmos.esa.int/web/xmm-newton/sas-thread-epic-filterbackground>

<sup>7</sup> [https://xmm-tools.cosmos.esa.int/external/xmm\\_user\\_support/documentation/uhb/epicintbkgd.html](https://xmm-tools.cosmos.esa.int/external/xmm_user_support/documentation/uhb/epicintbkgd.html).

<sup>8</sup> Ranalli et al. (2015).

<sup>9</sup> The 4'' pixel size is motivated by the 4.1'' PSF size of PN, see [https://xmm-tools.cosmos.esa.int/external/xmm\\_user\\_support/documentation/uhb/epicpsf.html](https://xmm-tools.cosmos.esa.int/external/xmm_user_support/documentation/uhb/epicpsf.html).

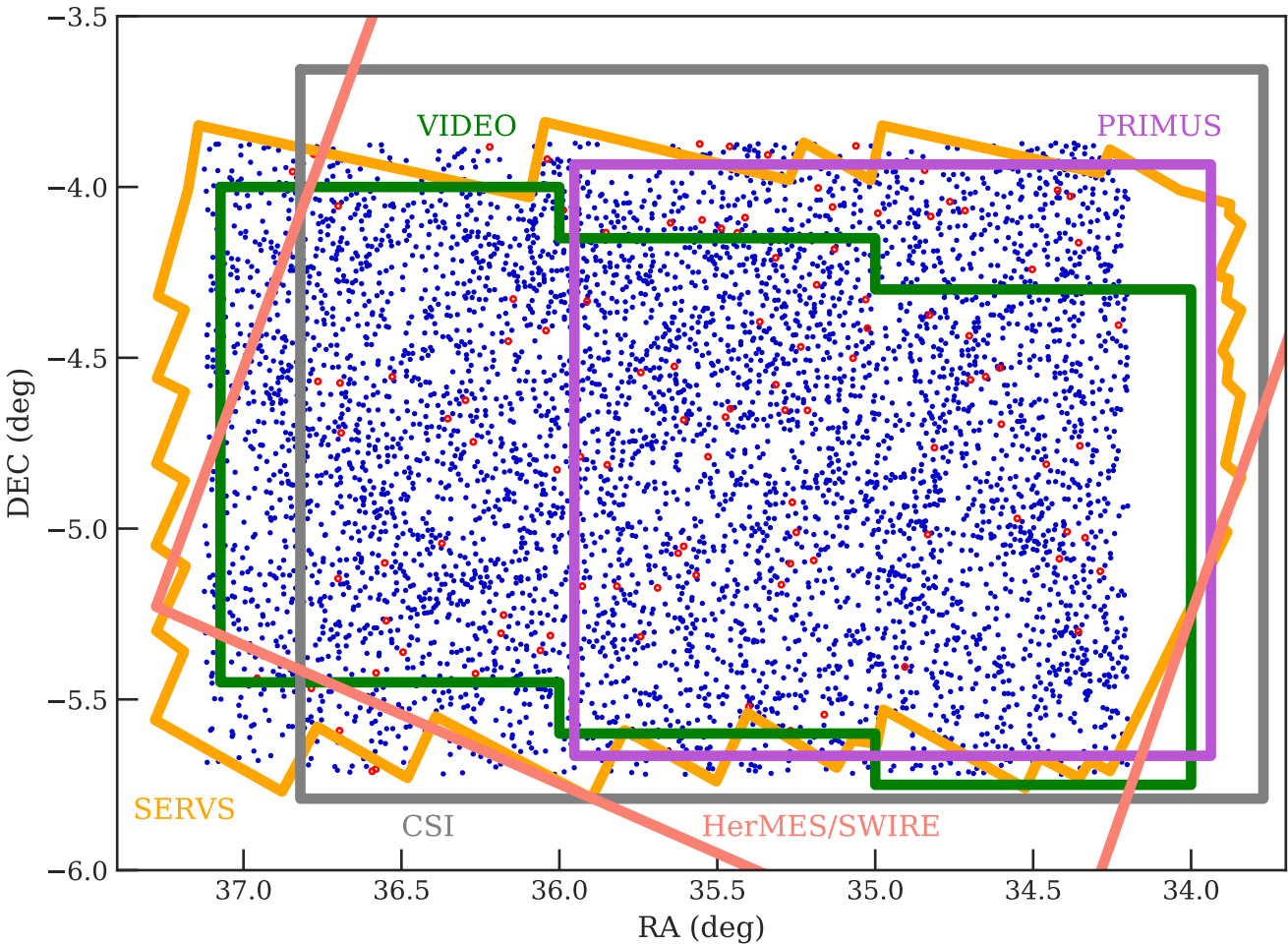


**Figure 3.** Spatial distribution of the 5252 sources detected in this work. We have identified reliable multiwavelength counterparts (see Sec. 5.1 and Sec. 5.2 for details) for 98% of the *XMM-Newton* sources (blue dots), while the remaining 2% of sources are marked as open circles. Some of the multiwavelength coverage of the XMM-LSS field is also shown as labeled (see §5 for details)

METHOD=MODEL. This option fits the source-excised image with two templates: the vignetted exposure map, and the un-vignetted exposure map. The former represents the cosmic X-ray background with an astrophysical origin, while the latter represents the intrinsic instrumental noise. ESNPLINEMAP then finds the best-fit linear combination of the two templates and generates a background map. The details of this method are described in Cappelluti et al. (2007). The background maps are used for the PSF-fitting based source detection task described in Step (iv).

- (iii) We run EWAVELET again for each observation. This time the source list is generated by running EWAVELET on the exposure map and image coadded across the PN, MOS1, and MOS2 exposures (when available) with the default likelihood threshold (THRESHOLD=5).
- (iv) For each EWAVELET source list, we use the SAS task EMLDETECT to re-assess the detection likelihood and determine the best-fit X-ray positions. EMLDETECT is a PSF-fitting tool which performs maximum-likelihood fits to the input source considering the *XMM-Newton* PSF, exposure values, and background levels of the input source on each image. EMLDETECT also convolves the PSF with a  $\beta$ -model bright-

ness profile<sup>10</sup> for clusters and uses the result to determine if the input source is extended. We use a stringent likelihood threshold (LIKMIN= 10.8) to ensure that astrometric corrections are calculated based on real detections, and we only keep the point sources.

- (v) For the mosaic-mode observations (see Footnote 2), the multiple pointings under the same ObsID were already registered on the same WCS frame the ObsID. Therefore, we do not correct the astrometry for each pseudo-exposure but only consider the astrometric offsets on an ObsID-by-ObsID basis. The source lists for the mosaic-mode observations were generated using the SAS task EMOSAIC\_PROC, which is a mosaic-mode wrapper for procedures similar to (i)-(iv) described above.

For steps (iv) and (v), the source searching was conducted simultaneously on the images of the three EPIC cameras as the astrometric offsets between PN, MOS1, and MOS2 are negligible. For each ObsID, we cross-correlate the high-confidence EMLDETECT list of point sources (with the

<sup>10</sup> <http://xmm-tools.cosmos.esa.int/external/sas/current/doc/emdletect/node3.html>.

EMLDETECT flag EXT=0) with the optical source catalog culled from the Hyper Suprime-Cam Subaru Strategic Program Public Data Release 1 (HSC-SSP; Aihara et al. 2017), which is an ultra-deep optical photometric catalog with sub-arcsec angular resolution. The astrometry of HSC-SSP is calibrated to the Pan-STARRS1  $3\pi$  survey and has a  $< 0.05''$  astrometric uncertainty. More details of the HSC-SSP catalog can be found in Aihara et al. (2017), and it is also briefly discussed in §5. For astrometric corrections, we limit the optical catalog to HSC sources with  $i = 18 - 23$  to minimize possible spurious matches due to faint source densities at  $i > 23$  and matches to bright stars that might have proper motions or parallaxes.

The offset between each ObsID and the HSC catalog is calculated based on a maximum-likelihood algorithm similar to the SAS task EPOSCORR. The major difference between our approach and EPOSCORR is that we use an iterative optimization approach compared to the grid-searching algorithm adopted by EPOSCORR. During each iteration, we cross-correlate the optical catalog with the X-ray catalog using a  $10''$  search radius and exclude all matches with multiple counterparts (less than 5% of our X-ray sources have more than one optical counterpart in the bright HSC-SSP catalog). We then calculate the required astrometric corrections that maximize the cross-correlation likelihood. After each iteration, we apply the best-fit astrometric offsets to the source list and next repeat the catalog cross-correlation steps and re-calculate the required additional corrections for the source list. The required astrometric corrections usually converge after 1–2 iterations. For the purpose of frame-correction, we adopt the X-ray positional uncertainties calculated based on the PSF-fitting likelihood ratios provided by EMLDETECT ( $\sigma_{eml}$  hereafter). The positional uncertainty information is necessary because the required astrometric corrections should be weighted by on X-ray sources with better positions within each observation. To avoid over-weighting sources with extremely small  $\sigma_{eml}$ , we also include a constant  $0.5''$  systematic uncertainty when calculating the best-fit values for frame-correction.<sup>11</sup> The median number of X-ray sources in an ObsID with only one HSC counterpart within  $3''$  is 32.

The required frame-correction offsets calculated using our approach are less than  $3''$  in both RA and DEC and are generally consistent with the results calculated using EPOSCORR, with a median difference of  $0.1''$ . For two ObsIDs the difference between our offsets and the EPOSCORR offsets are non-negligible ( $> 0.5''$ ). We visually inspect these ObsIDs and conclude that our approach does improve the alignments between the optical and corrected X-ray images. The event files and the attitude file for each ObsID are then projected onto the WCS frame of the HSC catalog by updating the relevant keywords using a modified version of ALIGN\_EVT (Ranalli et al. 2013). Since the sky coordinates for the event files of the mosaic-mode pseudo-pointings are derived based on the reference point centered at the nominal RA and DEC positions of the mosaic-mode ObsIDs, we also recalculate the sky coordinates for these event files with the SAS task ATTCALC using the true pointing positions as

<sup>11</sup> We assume the systematic uncertainties to be  $0.5''$  as suggested by Watson et al. (2008).

the reference point, which is necessary for using regular SAS tasks for mosaic-mode pseudo-exposures.

### 3.2 Second-pass source detection

We re-create images, exposure maps, detector masks, and background maps using the frame-corrected event files and attitude files. We then run source-detection tasks for the second time considering all *XMM-Newton* observations listed in Table 2. Similar to the approach used for the XMM-H-ATLAS survey (Ranalli et al. 2015), we divide the XMM-LSS field into a grid when running the second-pass source detection because the number of images that can be processed by a single EMLDETECT thread is limited. We use a custom-built wrapper of relevant SAS tasks to carry out the second-pass source detection, which is similar to the GRIDDETECT<sup>12</sup> tool built for the XMM-H-ATLAS survey (Ranalli et al. 2015).

The cell sizes of the grid are determined by the number of EWAVELET sources. For each cell in the grid, we co-add the images and exposure maps for all observations with footprint inside the cell and run EWAVELET with a low detection threshold<sup>13</sup> on the co-added image and exposure map. For each cell, we only keep EWAVELET sources within the RA/DEC range of the cell plus  $1'$  “padding” on each side of the cell. We then use the EWAVELET list as an input for EMLDETECT to assess the detection likelihood. Instead of running on the co-added image, EMLDETECT takes the image, exposure map, background map, and detector mask of each input observation into account. The EMLDETECT point-source list of the full XMM-LSS region is constructed from the union of the sources from all cells after removing duplicates due to the “padding”. We search for sources in three different bands: 0.5–2 keV (soft), 2–10 keV (hard), and 0.5–10 keV (full). We consider sources with EMLDETECT likelihood larger than DET<sub>ML</sub> = 6.0 to be reliably detected. This equivalent to a  $2.5 \times 10^{-3}$  probability of a detected sources being a random Poisson fluctuation of the background. A total of 5252 sources satisfy this criterion in at least one of the three bands (see §3.4). For readers interested in an even more reliable catalog, we suggest using the DET<sub>ML</sub> = 10.8 detection threshold (equivalent to a false-detection probability of  $2 \times 10^{-5}$ ) for the final X-ray catalog. A total of 4963 sources have DET<sub>ML</sub>  $\geq 10.8$  in at least one band. The detection thresholds are determined by extensive simulations that are discussed in §4. We show the spatial distribution of the 5252 detected sources in Fig. 3.

### 3.3 Astrometric accuracy

We investigate the positional accuracy of the *XMM-Newton* sources by comparing the second-pass X-ray catalog with the HSC-SSP catalog. Similar to the frame-correction procedures described in §3.1, we search for unique optical counterparts around the X-ray positions using a  $3''$  search radius. For the 5236 X-ray sources detected in the full-band during the second-pass source-searching process, a total of 2085 X-ray sources are found to have only one  $i = 18 - 23$

<sup>12</sup> <https://github.com/piero-ranalli/griddetect>.

<sup>13</sup> THRESHOLD=4.

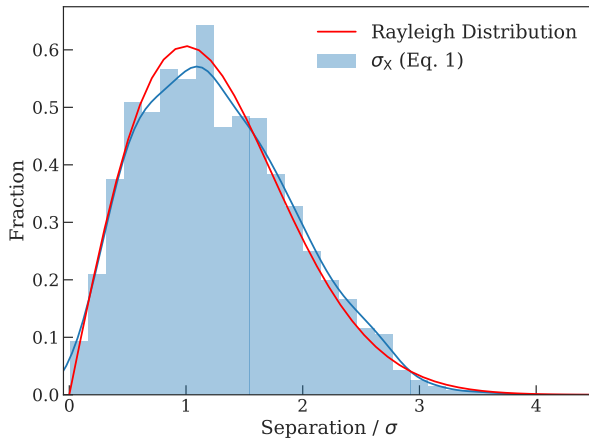


**Figure 4.** Histograms of the normalized full-band positional offsets, a dimensionless quantity defined as the positional offsets normalized by the empirically derived positional uncertainty; , and comparison with the expected Rayleigh distribution, the solid red curve. The kernel-density estimation of the normalized positional offset distribution is shown as the solid blue curve. The excellent agreement between the two distributions suggest that our empirically derived  $\sigma_x$  values are reliable indicators of the true positional uncertainties.

HSC counterpart within  $3''$ . We use the separations between the optical and X-ray positions of this subsample as a means to determine empirical X-ray positional uncertainties, which is a commonly adopted practice in deep X-ray surveys (e.g. Luo et al. 2010, 2017; Xue et al. 2011).

The X-ray positional accuracy is determined by how well the PSF-centroid location can be measured, which usually depends on the number of counts of the detected source and the PSF size of the instrument (primarily dependent on the off-axis angle). For the vast majority of the X-ray sources presented in this work, the detected photons are from at least three different observations, and hence the dynamical range of effective off-axis angle for each source detected on the coadded image is relatively small, and thus the X-ray positional uncertainty is mostly dependent on the number of counts available for detected sources. Using the angular separations between the 2085 X-ray sources and their unique optical counterparts, we derive an empirical relation between the number of X-ray counts,  $C$ ,<sup>14</sup> and the 68% positional-uncertainty radius ( $r_{68\%}$ ) for the full-band-detected X-ray sources,  $\log_{10} r_{68\%} = -0.31 \times \log_{10} C + 0.85$ . The parameters are chosen such that 68% of the sources have positional offsets smaller than the empirical relation.

For this work, we define the X-ray positional uncertainty,  $\sigma_x$ , to be the same as the uncertainties in RA and DEC where  $\sigma_{\text{RA}} = \sigma_{\text{DEC}} = \sigma_x$ . Under this definition,  $\sigma_x$  is  $r_{68\%}$  divided by a factor of 1.515 (e.g., Eq. 21 and §4.2 of Pineau et al. 2017). The factor 1.515 is determined by integrating the Rayleigh distribution until the cumulative probability reaches 0.68. For reference, 90%, 95%, and 99.73% uncertainties correspond to  $2.146\sigma_x$ ,  $2.448\sigma_x$ ,  $3.439\sigma_x$ , respectively. Because the separations in both RA and DEC behave as a

<sup>14</sup> An upper limit of 2000 is set on  $C$  because the improvement of positional accuracy is not significant for larger source counts (e.g., Luo et al. 2017).

univariate normal distribution with  $\sigma_{\text{RA}}$  and  $\sigma_{\text{DEC}}$ , respectively,<sup>15</sup> the angular separation should therefore follow the joint probability distribution function of the uncertainties in the RA and DEC directions. Since we assume  $\sigma_{\text{RA}} = \sigma_{\text{DEC}}$ , the angular separation between an optical source and an X-ray source should follow the univariate Rayleigh distribution with the scaling parameter  $\sigma_x$ , where  $\sigma_x = \sigma_{\text{RA}} = \sigma_{\text{DEC}}$  (see §4 of Pineau et al. 2017, for details).

For each energy band, we repeat the same process to find the best-fit relation for  $\sigma_x$  using the following equation:

$$\log_{10} \sigma_x = \alpha \times \log_{10} C + \beta. \quad (1)$$

Given the PSF size and positional accuracy of *XMM-Newton*, it is possible for X-ray sources to have angular separation from optical sources larger than  $3''$ , and the positional uncertainties derived based on counterparts found within the  $3''$  search radius can be underestimated. Therefore, we adopt an iterative process. For each iteration, we use the derived  $\sigma_x$  to identify reliable matches using the likelihood-ratio matching method described in §5.1. We then re-derive Eq. 1 using the reliable matches, and the updated astrometric uncertainties are used for running likelihood-ratio matching again. This is a stable process, as the parameters converge after 2–3 iterations. The average positional uncertainties ( $\sigma_x$ ) for our soft-band, hard-band, and full-band X-ray catalogs are  $1.^{\circ}35$ ,  $1.^{\circ}37$ , and  $1.^{\circ}31$ , respectively. Fig. 4 presents a comparison of the normalized separation (Separation/ $\sigma$ ) between the full-band X-ray sources and their bright optical counterparts with  $\sigma$  derived using Eq. 1,  $\sigma_x$ . The agreement between the Rayleigh distribution and the Separation/ $\sigma_x$  distribution of our sample demonstrates that our empirically derived  $\sigma_x$  values are reliable indicators of the true positional uncertainties. As for  $\sigma_{\text{eml}}$ , previous studies have reported that  $\sigma_{\text{eml}}$  can have unrealistically low values for on-axis sources with large numbers of counts, an irreducible systematic uncertainty should be added to  $\sigma_{\text{eml}}$  for the normalized separation to follow a Rayleigh distribution (e.g., Watson et al. 2008), but the nature of this systematic uncertainty remains unclear. For this work, we use  $\sigma_x$  as the positional uncertainties of our X-ray catalog, but  $\sigma_{\text{eml}}$  is also included in the final catalog for completeness.

### 3.4 The main X-ray source catalog

We detect 3951, 2691, and 5228 point sources with  $\text{DET\_ML} \geq 6.0$  in the 0.5–2 keV, 2–10 keV, and 0.5–10 keV bands, respectively. The details of the main X-ray source catalog are reported in Table A of Appendix A. The extended sources (identified by the  $\text{EXT} > 0$  flag of EMLDETECT) are not included, as the properties of the extended X-ray emission are beyond the scope of this work.<sup>16</sup> We combine catalogs from the three energy bands using a similar approach to

<sup>15</sup> Here we consider the positional uncertainties of the HSC-SSP catalog to be negligible compared to the *XMM-Newton* positional uncertainties.

<sup>16</sup> There are 68, 11, and 77 sources identified as  $\text{EXT} > 0$  by EMLDETECT in the 0.5–2 keV, 2–10 keV, and 0.5–10 keV bands, respectively. The properties of the extended sources will be reported in a separate work.

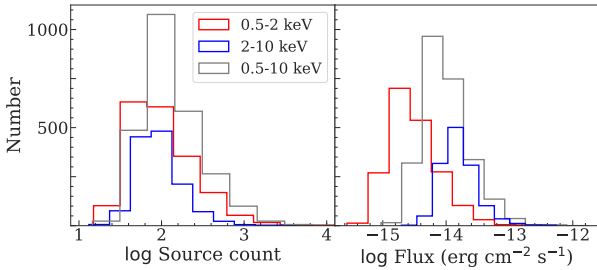


**Figure 5.** Left – Source-count distributions for the sources detected in the soft (red), hard (blue), and full (gray) bands. Right – Flux distributions of the sources detected in the three bands. Colors are the same as in the left panel.

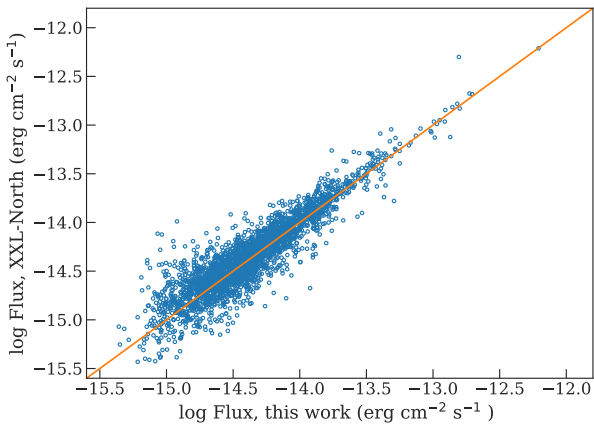


**Figure 6.** Comparison of the soft-band X-ray fluxes of our X-ray sources and those of the *XMM-Newton* counterparts identified in the XXL-North source catalogs (Liu et al. 2016) within a 10'' radius. As expected, almost all of the XXL-North X-ray sources in our catalog region can be matched to a counterpart in our X-ray source catalog with comparable flux.

that adopted by the *XMM-Newton* Serendipitous Source Catalogue. We consider two sources from different catalogs to be the same if their angular separation is smaller than any of the following quantities: (1) 10'', (2) distance to the nearest-neighbor in each catalog; or (3) quadratic sum of the 99.73% positional uncertainties from both bands. The final source catalog is the union of the sources detected in the three energy bands. We check for potential duplicate sources by visually inspecting all sources with distance to the nearest-neighbor (DIST\_NN) less than 10'', and only one set of sources is found to be duplicated, resulting in a total of 5252 unique sources. There are 2928 sources with more than 100 PN+MOS counts in the full-band, and 126 sources with more than 1000 X-ray counts. A unique X-ray source ID is assigned to each of the 5252 sources at this stage.

We also derive the count-rate to flux energy conversion factors (ECFs) assuming a power-law spectrum with photon index  $\Gamma = 1.7$ , which is typical for X-ray AGNs (e.g., Ranalli et al. 2015), and Galactic absorption. The energy ranges are those where the removed instrumental lines are excluded when deriving the ECFs. The conversion factors for PN and MOS are (6.57, 1.89), (1.25, 0.43), and (3.05, 0.90) counts s<sup>-1</sup>/10<sup>-11</sup>erg cm<sup>-2</sup> s<sup>-1</sup>, in the 0.5–2 keV, 2–10 keV, and 0.5–10 keV bands, respectively. For each source detected

by EMLDETECT, the flux from each EPIC camera is calculated separately using the corresponding ECF. The final flux of the source is the error-weighted mean of the fluxes from the three EPIC cameras, when available. The median fluxes for the soft, hard, and full bands are  $2.9 \times 10^{-15}$ ,  $1.5 \times 10^{-14}$ , and  $9.4 \times 10^{-15}$  erg cm<sup>-2</sup> s<sup>-1</sup>, respectively. The source-count and flux distributions of the sources detected in the three energy bands are displayed in Fig. 5.

For sources that are detected in fewer than three bands, we calculate the source-count upper limits using the mosaicked background map of the band in which the source is not detected. The mosaicked background map of each band is generated by summing the background maps from all individual observations (see §3.1). According to the Poisson probability set by the EMLDETECT detection likelihood threshold ( $P_{\text{Random}}$ , the probability of the detected source being a random Poisson fluctuation due to the background), we can calculate the minimum required total counts ( $m$  in the following equation) required to exceed the expected number of background counts,  $B$ , using the regularized upper incomplete  $\Gamma$  function (which is equivalent to Eq. 2 of Civano et al. (2016) if  $m$  is a positive integer):

$$P_{\text{Random}} = \frac{1}{\Gamma(m)} \int_B^\infty t^{m-1} e^{-t} dt \quad (2)$$

The upper limits are set at  $P_{\text{Random}} = 2.5 \times 10^{-3}$  (consistent with DET\_ML=6). For each non-detected source in each band, we determine the background counts by summing the background map within the circle with 70% encircled energy fraction (EEF). We then calculate  $m$  by solving Eq. 2 using the SCIPY function SCIPY.SPECIAL.GAMMAINCINV.<sup>17</sup> Since  $m$  is the required *total* counts to exceed random background fluctuations at the given probability, the flux upper limit is calculated based on the following equation, which is similar to Equation 2 of Cappelluti et al. (2009) and Equation 2 of Civano et al. (2016):

$$S = \frac{m - B}{t_{\text{exp}} \times \text{EEF} \times \text{ECF}}. \quad (3)$$

Here EEF corrects for PSF loss and is 0.7, and  $t_{\text{exp}}$  is the median exposure time within the 70% EEF circle. The flux upper limits are calculated as the exposure-time-weighted mean of the three EPIC detectors.

For each source detected in either the soft or the hard band (or both), we calculate its hardness ratio (HR), defined as  $(H - S)/(H + S)$ , where  $H$  and  $S$  are the source counts weighted by the effective exposure times in the hard and the soft bands, respectively. The source counts are the default output of EMLDETECT, which is the sum of the counts from all three EPIC detectors. We report this value in our catalog for direct comparison with previous studies. The uncertainties on HR are calculated based on the count uncertainties from the output of EMLDETECT using the error propagation method described in §1.7.3 of Lyons (1991).

As a comparison, a total of 2866 X-ray sources from XXL-North (Liu et al. 2016) are found to have a counterpart within the 10'' radius in our X-ray catalog. For these

<sup>17</sup> This quantity is the inverse function of Eq. 2.

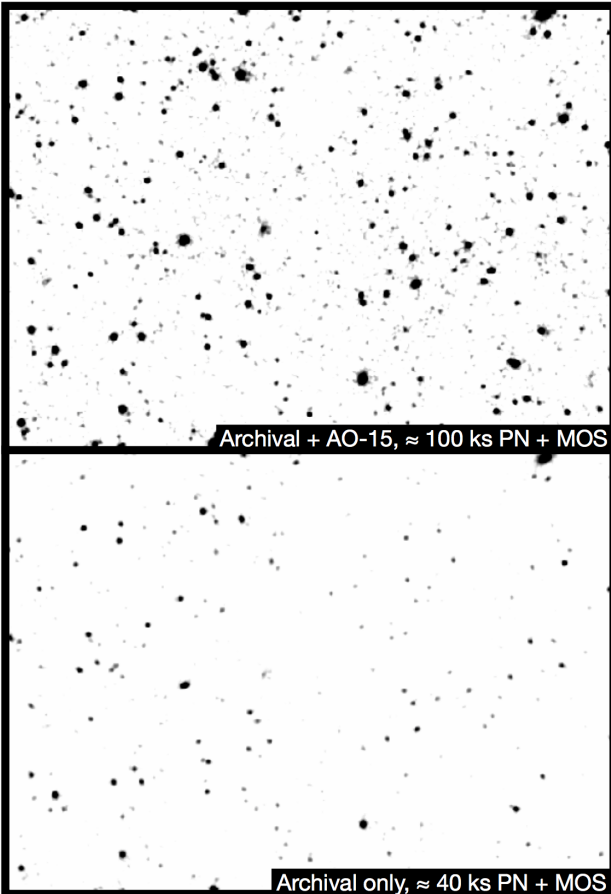


**Figure 7.** Top – Background-subtracted, smoothed, and coadded PN+MOS image in the 0.5–10 keV band for a  $0.8 \times 0.6 \text{ deg}^2$  region centered at  $\text{RA}=35.58^\circ$ ,  $\text{DEC}=-4.965^\circ$ . This image is created using both archival data and the new AO-15 data, a total of 862 sources are detected in this region. Bottom – Same as the top image, but only the archival data are included. The two images are matched in color scale. In the Liu et al. (2016) catalog, only 581 sources can be found in this region. The typical vignetting-corrected exposure times are shown at the bottom of both panels. The exposure time of the full survey region is shown in Fig. 2.

matched sources, we show the comparison between the soft-band X-ray fluxes reported in the XXL-North catalog and those in our catalog in Fig. 6. As expected, the majority of the archival sources detected in our catalog have consistent soft-band fluxes. Since the SXDS observations were also used for constructing the XXL-North (Liu et al. 2016) catalog, the 2866 sources matched to the XXL-North catalogs are considered to be matched to all available archival sources, and conclude that the other 2386 X-ray sources in our catalogs to be new sources. We include the IDs from the Liu et al. (2016) catalog for these matched objects in our source catalog (Table A). In our source-detection region, 172 sources from the original (Liu et al. 2016) catalog do not have a counterpart in our point-source catalog. Of these 172 sources, 150 can be associated with the extended sources or  $\text{DET\_ML} < 6.0$  sources excluded from our point-source catalog (see §3.2). The remaining sources comprise  $< 1\%$  of the XXL-North catalog in our source-detection region. Visual inspection suggests that the vast majority of

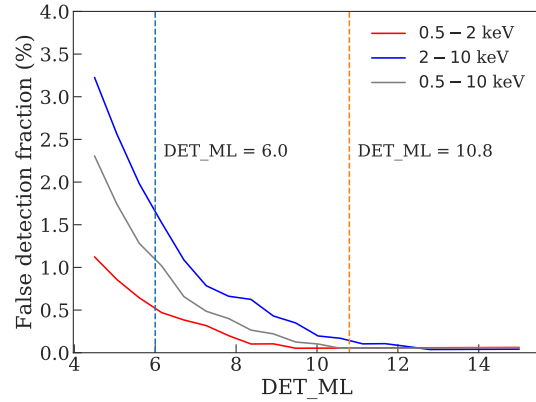


**Figure 8.** The fraction of spurious sources detected at different  $\text{DET\_ML}$  based on simulations. The detection thresholds relevant to our catalog are marked as the vertical dashed lines.

these sources might be spurious detections, but we cannot rule out the possibility that some sources are missed in our catalog due to X-ray variability (e.g., Yang et al. 2016). Also, the XXL-North catalog adopted a different source detection approach (see §2 of Liu et al. 2016 for details.) The properties of sources that exhibit strong X-ray variability will be presented in a separate work. Fig. 7 shows the background-subtracted, 0.5–10 keV PN+MOS image (see §3 for the details of data analysis) from a  $\approx 0.5 \text{ deg}^2$  region in XMM-LSS generated using the combined AO-15 and archival data. An image produced using only the archival data is also displayed for comparison, demonstrating the improved source counts with the additional AO-15 observations.

## 4 SURVEY SENSITIVITY AND $\log N - \log S$

### 4.1 Monte Carlo simulation

To assess our survey sensitivity, we perform Monte Carlo simulations of X-ray observations. For each simulation, we generate a list of mock X-ray sources by sampling from the  $\log N - \log S$  relations reported in the XMM-COSMOS survey (Cappelluti et al. 2009, for the 0.5–2 keV and 2–10 keV bands) and the *Chandra* Multiwavelength Project survey (ChaMP; Kim et al. 2007, for the 0.5–10 keV band). The maximum flux of the mock X-ray catalogs is set at  $10^{-11} \text{ erg cm}^{-2} \text{ s}^{-1}$ . The minimum flux of the mock X-ray sources at each energy band is set as 0.5 dex lower than the minimum detected flux (e.g. LaMassa et al. 2016). We randomly place the mock X-ray sources in the RA/DEC range covered by the *XMM-Newton* observations used in this work. We then use a modified version of the simulator written for the *XMM-Newton* survey of the CDF-S (Ranalli et al. 2013), CDFS-SIM,<sup>18</sup> to create mock event files. CDFS-SIM converts X-ray fluxes to PN and MOS count rates with the same model used for deriving the ECFs, and it then randomly places X-ray events around the source location according to

<sup>18</sup> <https://github.com/piero-ranalli/cdfs-sim>

**Table 3.** Sensitivity curves. Column 1: Soft-band flux. Column 2: Soft-band survey solid angle ( $\text{DET\_ML} = 6$ ). Column 3: Soft-band survey solid angle ( $\text{DET\_ML} = 10.8$ ). Columns 4–6: Similar to Columns 1–3 but for the hard band. Columns 7–9: Similar to Columns 1–3 but for the full band. This table is available in its entirety online.

$\log S_{0.5-2\text{keV}}$ (erg cm $^{-2}$ s $^{-1}$ )	$\Omega_{0.5-2\text{keV}}^6$ (deg $^2$ )	$\Omega_{0.5-2\text{keV}}^{10.8}$ (deg $^2$ )	$\log S_{2-10\text{keV}}$ (erg cm $^{-2}$ s $^{-1}$ )	$\Omega_{2-10\text{keV}}^6$ (deg $^2$ )	$\Omega_{2-10\text{keV}}^{10.8}$ (deg $^2$ )	$\log S_{0.5-10\text{keV}}$ (erg cm $^{-2}$ s $^{-1}$ )	$\Omega_{0.5-10\text{keV}}^6$ (deg $^2$ )	$\Omega_{0.5-10\text{keV}}^{10.8}$ (deg $^2$ )
(1)	(2)	(3)	(4)	(5)	(6)	(7)	(8)	(9)
−15.40	1.855	0.044	−14.53	0.826	0.038	−14.81	0.782	0.038
−15.38	2.129	0.055	−14.51	1.040	0.046	−14.80	0.999	0.046
−15.37	2.391	0.069	−14.50	1.277	0.054	−14.78	1.243	0.055
−15.35	2.633	0.082	−14.48	1.524	0.063	−14.77	1.491	0.065
−15.34	2.856	0.098	−14.47	1.790	0.074	−14.75	1.763	0.078

the count rates, the *XMM-Newton* PSFs at the given off-axis angle, and the real exposure maps. We extract images from the simulated event files using the same methods described in §3. For each observation, the simulated image is combined with a simulated background, which is created by re-sampling the original background map according to Poisson distributions to create simulated images that mimic the real observations. For each energy band, a total of 20 simulations are created.

We run the same two-stage source-detection procedures described in §3 on the simulated data products. For each simulation, we match the detected sources to the input sources within a  $10''$  search radius by minimizing the quantity  $R^2$ :

$$R^2 = \left( \frac{\Delta \text{RA}}{\sigma_{\text{RA}}} \right)^2 + \left( \frac{\Delta \text{DEC}}{\sigma_{\text{DEC}}} \right)^2 + \left( \frac{\Delta \text{RATE}}{\sigma_{\text{RATE}}} \right)^2. \quad (4)$$

Here  $\Delta \text{RA}$  and  $\Delta \text{DEC}$  are the differences between the simulated RA/DEC positions and the RA/DEC positions obtained by running source detection on the simulated images.  $\Delta \text{RATE}$  is the difference between the simulated count rates and the detected count rates.  $\sigma_{\text{RA}}$ ,  $\sigma_{\text{DEC}}$ , and  $\sigma_{\text{RATE}}$  are the uncertainties of RA, DEC, and count rates of the detected sources. Minimizing  $R^2$  takes into account the flux and positional differences between the input catalog and the sources detected in the simulated images (e.g., Cappelluti et al. 2007; Ranalli et al. 2015). Detected sources without any input sources within the  $10''$  radius are considered to be spurious detections.

Fig. 8 presents the spurious fraction as a function of  $\text{DET\_ML}$  for the soft, hard, and full bands. For our catalog, we consider sources with  $\text{DET\_ML} > 6$  to be reliably detected. At this threshold, the spurious fractions are 0.73%, 2.01%, and 1.68% for the soft, hard, and full bands, respectively. For the threshold at  $\text{DET\_ML} = 10.8$ , the spurious fractions become 0.08%, 0.34%, and 0.10%, respectively. The low spurious fraction in the soft-band is likely due to its lower background levels. For the full X-ray source catalog of 5252 sources, these spurious fractions translate to  $\approx 88$  spurious detections for  $\text{DET\_ML} > 6$ , and  $\approx 5$  spurious detections for the 4908  $\text{DET\_ML} > 10.8$  sources.

#### 4.2 Survey sensitivity, sky coverage, and $\log N - \log S$

We create sensitivity maps of our survey region in different bands using the background and exposure maps generated as described in §2.2. The mosaicked background and exposure

maps are binned to  $5 \times 5$  pixels ( $20'' \times 20''$ ). For each pixel of the binned, mosaicked background map, the minimum required source counts to exceed the random background fluctuations are calculated using Eq. 2. The sensitivity is then calculated using Eq. 3 with the corresponding EEF and ECF values. The soft-band sensitivity map is presented in Fig. 9-left. We also generated a soft-band sensitivity map using only the archival data. To visualize the improvement upon the archival data, we compare the full-band sky coverage obtained from all available *XMM-Newton* data in our survey region with the sky coverage obtained using only the archival data. Fig. 9-right demonstrates the improved survey depth and uniformity with the new *XMM-Newton* observations. The sky coverage corresponding to the  $\text{DET\_ML} \geq 6.0$  catalog in our survey region in the soft, hard, and full-bands is shown in Fig. 10. The sensitivity curves for both the  $\text{DET\_ML} \geq 6.0$  and  $\text{DET\_ML} \geq 10.8$  catalogs are presented in Table 3.

We calculate the  $\log N - \log S$  relations of our survey using the sky coverage curves described above and the following equation:

$$N(> S) = \sum_{i=1}^{N_s} \frac{1}{\Omega_i}. \quad (5)$$

Here  $N(> S)$  represents the total number of detected sources with fluxes larger than  $S$ , and  $\Omega_i$  is the sky coverage associated with the flux of the  $i$ th source. The  $\log N - \log S$  relations of our survey are shown in Fig. 11, along with the  $\log N - \log S$  relations for a selection of surveys spanning a wide range of area and sensitivity. The flux differences caused by different choices of power-law indices and/or slight differences in energy ranges have been corrected assuming a  $\Gamma = 1.7$  power-law spectrum adopted in this work. Considering factors such as different spectral models and/or methods of generating survey sensitivity curves, our  $\log N - \log S$  relations are consistent with the relations reported in the literature.

#### 5 MULTIWAVELENGTH DATA IN THE XMM-LSS FIELD

The XMM-LSS region is one of the most extensively observed extragalactic fields. The publicly available multiwavelength observations in the XMM-LSS region utilized in this work are SERVS (Mauduit et al. 2012), SWIRE (Lonsdale et al. 2003), VIDEO (Jarvis et al. 2012), the CFHTLS-wide survey (Hudelot et al. 2012), and the HSC-SSP survey (Aihara et al. 2017).

We focus on identifying the correct counterparts for our

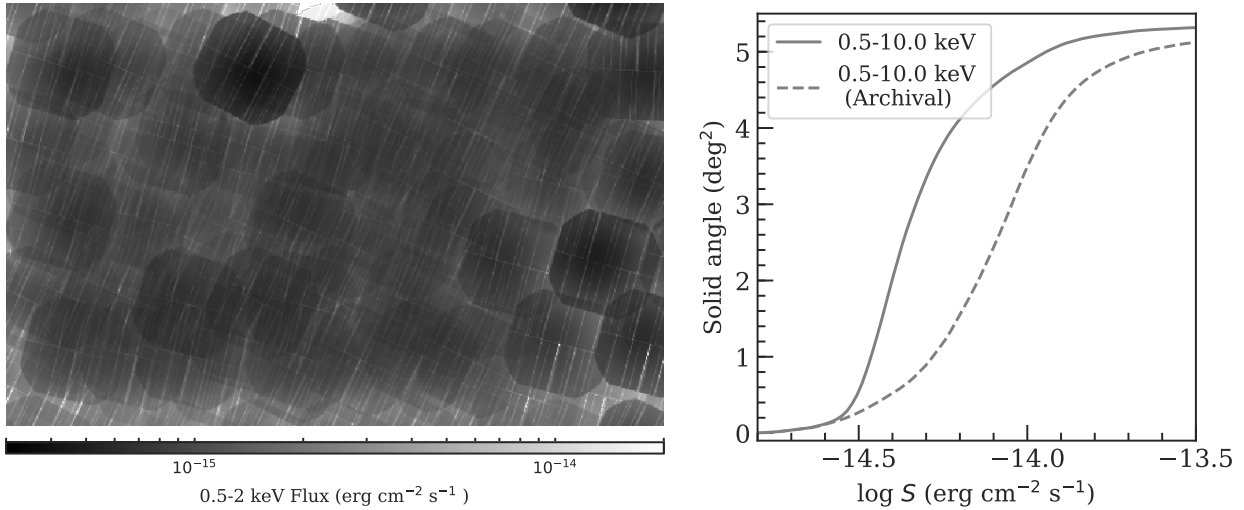


**Figure 9.** *Left* – Soft-band sensitivity map of the source-detection region (the same as the cyan box shown in Fig. 2). *Right* – Comparison of the full-band sky coverages between this work (solid line) and the archival *XMM-Newton* observations (dashed line), demonstrating the improved and more uniform sensitivity across the wide field enabled by the new data.

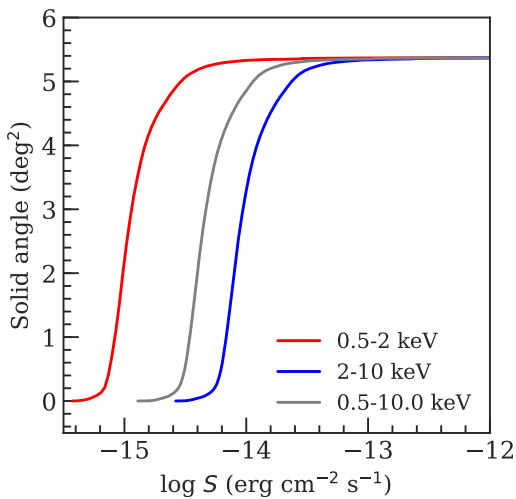


**Figure 10.** Sky coverage in the soft, hard, and full bands of our X-ray survey in XMM-LSS.

X-ray sources in four deep optical-to-near-IR (OIR) catalogs: SERVS, VIDEO, CFHTLS, and HSC-SSP. SERVS is a post-cryogenic *Spitzer* IRAC survey in the near-IR 3.6 and 4.5  $\mu$ m bands with  $\approx 2\mu$ Jy survey sensitivity limits and  $\approx 5$  deg $^2$  solid-angle coverage in the XMM-LSS region. We make use of the highly reliable two-band SERVS catalog built using SExtractor, obtained from the *Spitzer* Data Fusion catalog,<sup>19</sup> which has  $\approx 4 \times 10^5$  sources. The Spitzer Data Fusion catalog has already integrated data from SWIRE, which include photometry in all four IRAC bands and the photometry in MIPS 24, 70, and 160  $\mu$ m. A total of 82% of the X-ray sources (93% of the X-ray sources with SERVS coverage) have at least one SERVS counterpart candidate within their 99.73% positional-uncertainty radius ( $r_{99\%}$  hereafter), which

is equivalent to  $3.44\sigma_x$ ), which is calculated based on the quadratic sum of the 99.73% X-ray positional uncertainties and the corresponding OIR positional uncertainties.

VIDEO is a deep survey in the near-infrared  $Z$ ,  $Y$ ,  $J$ ,  $H$ , and  $K_s$  bands with  $\approx 80\%$  completeness at  $K_s < 23.8$ . In the XMM-LSS region, VIDEO covers a 4.5 deg $^2$  area ( $\approx 85\%$  of our X-ray survey region) with a total of  $\approx 5.7 \times 10^5$  sources; 79% of the X-ray sources (93% of the X-ray sources with VIDEO coverage) have at least one VIDEO counterpart candidate within  $r_{99\%}$ .

The CFHTLS-W1 survey covers the entirety of our X-ray data, with an 80% completeness limit of  $i' = 24.8$ . We select the CFHTLS sources in the RA/DEC ranges marginally larger (1') than our source-detection region. We limit the CFHTLS sources to those with  $SNR > 5$  in the  $i'$ -band. The total number of sources in the  $i'$ -band selected catalog is  $\approx 8.1 \times 10^5$ . A total of 90% of the X-ray sources in our catalog have at least one CFHTLS counterpart candidate within  $r_{99\%}$ .

The XMM-LSS field is entirely encompassed by the 108 deg $^2$  HSC-SSP wide survey. The limiting magnitude in the  $i$ -band for the wide HSC-SSP survey is 26.4. Inside the XMM-LSS field, HSC-SSP also has “ultra-deep” ( $\approx 1.77$  deg $^2$ ) and “deep” ( $\approx 5$  deg $^2$ ) surveys, which overlap with the SXDS and XMDS regions, respectively. We focus only on the wide survey because it is only 0.1 mag shallower than the deep survey in the  $i$ -band; and the uniform coverage is important for determining the background source density when matching to the X-ray catalog (see §5.1). We select the  $i$ -band detected HSC-SSP sources in the RA/DEC ranges slightly larger than our source-detection region<sup>20</sup>. The total number of HSC-SSP sources in our source-detection region

<sup>19</sup> <http://www.mattivaccari.net/df/>.

<sup>20</sup> We select sources with the DETECT\_IS\_PRIMARY and IDETECTED\_NOTJUNK flags set as TRUE, and CENTROID\_SDSS\_FLAGS set as FALSE. According to the HSC-SSP example script for selecting “clean objects”, we also exclude the HSC sources with FLAGS\_PIXEL\_EDGE, FLAGS\_PIXEL\_SATURATED\_CENTER,

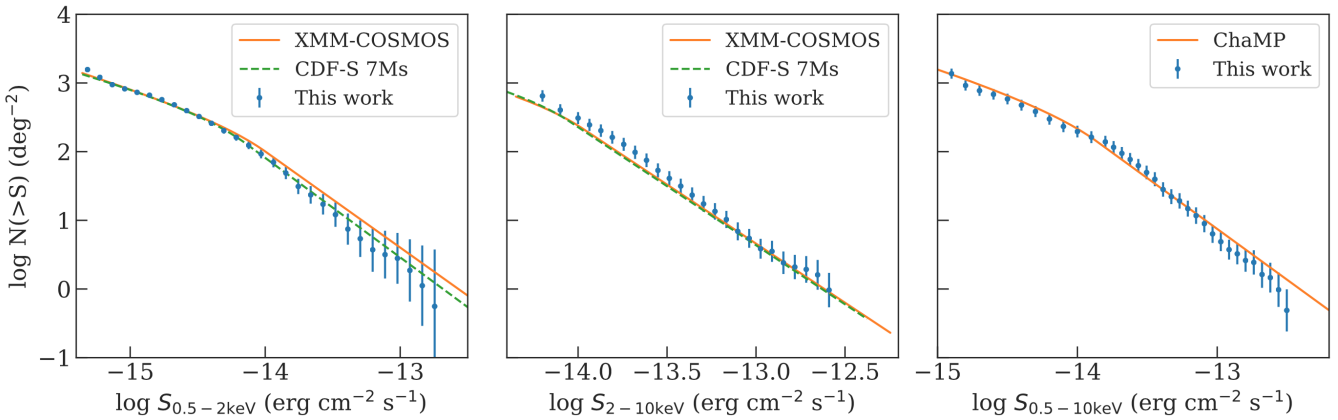


**Figure 11.** The  $\log N - \log S$  relations for our catalog in the soft-band (left), hard-band (middle), and full-band (right). The error bars represent the  $1\sigma$  uncertainties obtained using Eq. 4 of Cappelluti et al. (2009). For comparison, a few  $\log N - \log S$  relations from the literature with appropriate energy range and power-law index correction are shown. The  $\log N - \log S$  relations of our survey are generally consistent with previous studies.

is  $\approx 3.1 \times 10^6$ , and  $\approx 93\%$  of the X-ray sources in our main catalog have at least one HSC-SSP counterpart candidate within  $r_{99\%}$ .

Although CFHTLS is not as deep as HSC-SSP in the  $g$ ,  $r$ ,  $i$ , and  $z$  bands, it has complementary  $u^*$ -band photometry. Including photometry from both optical surveys also ensures that we will minimize the risk of missing an optical counterpart due to bad photometry caused by artifacts such as satellite tracks in either survey.

Since there are small systematic offsets in the astrometry of each catalog, we match SERVS, VIDEO, and CFHTLS to the HSC-wide catalog, and correct for the small offsets between each catalog to the HSC-wide catalog to maximize the counter-part matching accuracy. In the RA direction, the adopted corrections are  $0.020''$ ,  $0.027''$ , and  $0.026''$  for SERVS, VIDEO, and CFHTLS, respectively. For DEC, the adopted corrections are  $-0.009''$ ,  $-0.006''$ ,  $-0.008''$  for SERVS, VIDEO, and CFHTLS, respectively.

### 5.1 The likelihood-ratio matching method

To match reliably the X-ray sources to the OIR catalogs with much higher source densities, we employ the likelihood-ratio method (LR hereafter) similar to previous deep X-ray surveys, (e.g., Brusa et al. 2007; Luo et al. 2010, 2017). The likelihood ratio is defined as the ratio between the probability that the source is the correct counterpart, and the probability that the source is an unrelated background object (Sutherland & Saunders 1992):

$$LR = \frac{q(m)f(r)}{n(m)}. \quad (6)$$

Here  $q(m)$  is the magnitude distribution of the expected counterparts in each OIR catalog,  $f(r)$  is the probability distribution function of the angular separation between X-ray and OIR sources, and  $n(m)$  is the magnitude distribution of the background sources in each OIR catalog.

FLAGS\_PIXEL\_CR\_CENTER, FLAGS\_PIXEL\_BAD flags in the  $i$ -band to avoid unreliable  $i$ -band sources.

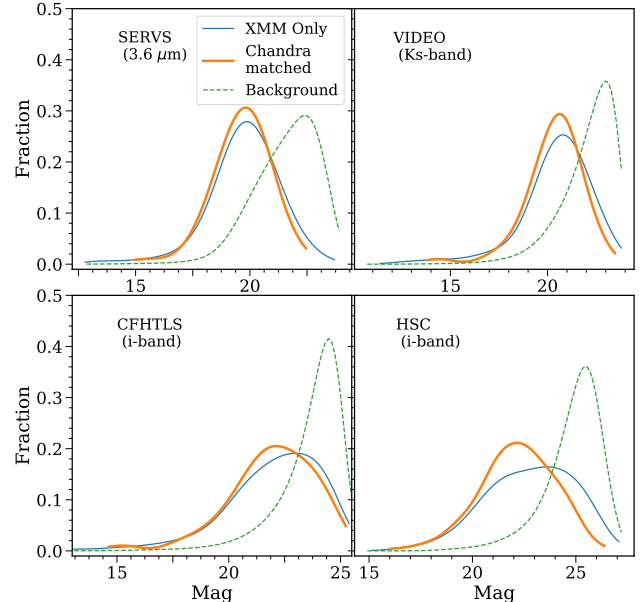


**Figure 12.** Kernel-density estimations of the magnitude distributions (solid lines) for the expected counterparts in SERVS (top-left), VIDEO (top-right), CFHTLS (bottom-left), and HSC-SSP (bottom-right). We show the distributions obtained using the full *XMM-Newton* catalog ( $q(m)_{XMM-Newton}$ ), and the distributions obtained using the *Chandra* sources in the XMM-LSS field ( $q(m)_{Chandra}$ ). The magnitude distributions of the background, unrelated sources are also displayed in each panel as the dashed curves. This figure demonstrates that  $q(m)_{Chandra}$  significantly improves upon the background-dominated  $q(m)_{XMM-Newton}$  for the deep OIR catalogs in the bottom panels.

We calculate the background source magnitude distributions using OIR sources between  $10''$  and  $50''$  from any sources in our X-ray catalog.

As discussed in §3.3, the probability distribution func-

tion of the angular separation should follow the Rayleigh distribution:

$$f(r) = \frac{r}{\sigma_x^2} \exp^{-\frac{r^2}{2\sigma_x^2}}. \quad (7)$$

Note that Eq. 7 is different from the two-dimensional Gaussian distribution function that maximizes at  $r=0$ , and thus the  $LR$  values calculated in this work are not directly comparable to previous works that adopted a Gaussian  $f(r)$ .

In practice, for an X-ray source with a total of  $N_c$  counterpart candidates within the search radius, the matching reliability for the  $i$ -th counterpart candidate  $MR_i$ , can be determined using the following equation:

$$MR_i = \frac{LR_i}{\sum_{k=0}^{N_c} LR_k + (1-Q)} \quad (8)$$

Here  $Q$  is the completeness factor, which is defined as  $Q = f_{m_{\text{lim}}}^{\infty} q(m)$ , where  $m_{\text{lim}}$  is the limiting magnitude of the OIR catalog being matched to. For each counterpart candidate,  $MR$  is equivalent to the relative matching probability among all possible counterpart candidates. See Eq. 5 of [Sutherland & Saunders \(1992\)](#) and §2.2 of [Luo et al. \(2010\)](#) for details.

Due to the relatively large positional uncertainties of *XMM-Newton* and the high source densities of the OIR catalogs, deriving an accurate magnitude distribution of the expected counterparts,  $q(m)$ , using *XMM-Newton* data is challenging. Therefore, we obtain  $q(m)$  for our X-ray sources by first matching our *XMM-Newton* catalog to the *Chandra* Source Catalog 2.0 (CSC 2.0; [Evans et al. 2010](#)) to take advantage of the higher angular resolution and positional accuracy of *Chandra*. We derive the positional uncertainties of the *Chandra* sources in our survey region using the same empirical approach described in [Xue et al. \(2011\)](#) by selecting CSC sources in the RA/DEC range of our catalog, and matching them onto HSC-SSP using a  $1.5''$  radius. We select CSC sources that are uniquely matched to our X-ray catalogs within the 95% uncertainties (*Chandra* and *XMM-Newton* positional uncertainties are added in quadrature). A total of 223 sources in our *XMM-Newton* catalog are matched to a unique *Chandra* source in the CSC. We match these *Chandra* sources to the four OIR catalogs using Eq. 6, with  $q(m)$  derived using the iterative approach described in [Luo et al. \(2010\)](#), which determines the  $LR$  threshold by optimizing the matching reliability and completeness. The  $q(m)$  derived from the CSC sources,  $q(m)_{\text{Chandra}}$ , is then used as the expected magnitude distribution for OIR counterparts of our *XMM-Newton* sources. The X-ray flux distributions in the soft, hard, and full bands of the *Chandra*-matched subsample are similar to those of our entire *XMM-Newton* catalog, and therefore  $q(m)_{\text{Chandra}}$  should be consistent with the intrinsic magnitude distributions of the real OIR counterparts of our full X-ray catalog. The counterpart-matching processes are run on four different OIR catalogs: SERVS, VIDEO, CFHTLS, and HSC-SSP. The details of the filters and apertures of the photometry in each OIR catalog can be found in Appendix A, where we give the descriptions of the columns reported in the source catalog (Columns 113–180 of Table A). For illustration, Fig. 12 shows the magnitude distributions of the background sources and the distributions of the expected counterparts derived using CSC sources.

For comparison, we also obtain  $q(m)$  for the full

*XMM-Newton* catalog without using the *Chandra* positions,  $q(m)_{\text{XMM-Newton}}$ . We again use the [Luo et al. \(2010\)](#) iterative method, but with a  $3''$  initial search radius.  $q(m)_{\text{XMM-Newton}}$  is also plotted on Fig. 12. It is evident that for ultra-deep OIR catalogs such as HSC-SSP and CFHTLS,  $q(m)_{\text{XMM-Newton}}$  is skewed toward the faint background sources compared to the *Chandra*-matched subsample. For the other catalogs, we find no qualitative difference between  $q(m)_{\text{Chandra}}$  and  $q(m)_{\text{XMM-Newton}}$ , but we still use  $q(m)_{\text{Chandra}}$  for consistency.

We next compute the  $LR$  values for all OIR sources within a  $10''$  radius (i.e., the counterpart “candidates”) of the X-ray sources using Eq. 6. For each OIR catalog, we choose the  $LR$  thresholds ( $LR_{\text{th}}$ ) such that the reliability and completeness parameters are maximized (see Eq. 5 of [Luo et al. 2010](#) for details). Counterparts with  $LR > LR_{\text{th}}$  are considered to be reliably matched. The results are reported in Table 4. For each OIR catalog, we list the number of all X-ray sources with at least one OIR counterpart candidate within  $r_{99\%}$  of the X-ray sources,  $N_{\text{All}}$ , and the number of X-ray sources with at least one reliably matched source with  $LR > LR_{\text{th}}$ ,  $N_{\text{Reliable}}$ . For an X-ray source with only one OIR counterpart candidate within the search radius but where its matching  $LR$  is smaller than  $LR_{\text{th}}$ , we consider the counterpart candidate to be an acceptable match if the separation from the OIR position to the X-ray position is less than  $r_{99\%}$ . The total number of such cases for each OIR catalog is listed as  $N_{\text{Acceptable}}$  in Table 4.

Motivated by the size of the spurious-matching rates (see §5.2 for the cross-matching reliability analysis), we first select a “primary” counterpart for each X-ray source from, in priority order, SERVS, VIDEO, CFHTLS, and HSC-SSP. After selecting the primary OIR counterpart, we associate different OIR catalogs with each other using a simple nearest-neighbor algorithm. Thanks to the much smaller positional uncertainties of the OIR catalogs, we adopt a constant search radius of  $1''$  for the OIR catalog associations, which is the approach used by the *Spitzer* Data Fusion database ([Vaccari 2016](#)).

Using this approach, 4913 ( $\approx 93\%$ ) X-ray sources have at least one robust counterpart with  $LR > LR_{\text{th}}$ . We consider an additional 23 X-ray sources without any counterpart candidates having  $LR > LR_{\text{th}}$  to have “acceptable” matches because there is only one unique counterpart in all OIR catalogs considered within  $r_{99\%}$ . When consider both the  $LR > LR_{\text{th}}$  counterparts and the acceptable counterparts, 4936 X-ray sources in our catalog are considered to have reliable OIR counterparts (94%). Of these sources, 4011 are matched to SERVS, 370 are from VIDEO, 376 are from CFHTLS, and 179 are from HSC. There are also 1068 sources with multiple counterparts having  $LR > LR_{\text{th}}$  and  $LR > 0.5LR_{\text{primary}}$  in various OIR catalogs. For these sources, we select a “secondary” counterpart based on the following priority order: (1) 239 best matches from VIDEO (2) 48 second-best matches from SERVS, (2) 77 second-best matches from VIDEO, (3) 287 best matches from CFHTLS, (4) 238 best matches from HSC, (5) 86 second-best matches from CFHTLS; and (6) 93 second-best matches from HSC. Finally, there are 29 X-ray sources with three reliable counterparts; these tertiary counterparts are from VIDEO (4), CFHTLS (6) and HSC (19). We note that the vast majority ( $\approx 85\%$ ) of X-ray sources with secondary and/or tertiary counterparts have a primary

**Table 4.** *LR* counterpart-matching results. Column 1: Catalog name. Column 2: Survey magnitude limit for each catalog in AB. Column 3: Survey area. Column 4: Positional uncertainty for each OIR catalog. Column 5: *LR* threshold. Column 6: Total number of X-ray sources with at least one counterpart within the  $10''$  search radius in each catalog. Column 7: Average number of OIR sources within  $r_{99\%}$  of the X-ray sources. The summary row shows the total number of X-ray sources with at least one OIR counterpart within  $r_{99\%}$ . Column 8: Total number of X-ray sources with at least one counterpart with  $LR > LR_{th}$ . Column 9: Total number of X-ray sources without any  $LR > LR_{th}$  counterpart candidates but having only one OIR source within  $r_{99\%}$ . The summary row displays the number of X-ray sources having only one unique OIR counterpart in all OIR catalogs considered within  $r_{99\%}$ , but the *LR* values do not exceed the reliability thresholds in all OIR catalogs. Columns 10–12: See §5.2 for details. Column 10: The fraction of X-ray sources in the “associated population” based on the results of Monte Carlo simulations. Column 11: false-matching rates determined using Monte Carlo simulations. Column 12: Fraction of the X-ray sources having identical reliable counterparts found based on their *Chandra* and *XMM-Newton* positions. For the summary row, Columns 10–12 are calculated as the weighed sum (based on the number of primary counterparts from each catalog) of the results from all four OIR catalogs.

Catalog	Limiting Magnitude	Area deg $^2$	$\sigma$	$LR_{th}$	$N_{\text{All}}$	$\bar{N}_{99\%}$	$N_{\text{Reliable}}$	$N_{\text{Acceptable}}$	$f_{\text{AP}}$	False Rate (Simulation)	Identical Fraction ( <i>Chandra</i> )
(1)	(2)	(3)	(4)	(5)	(6)	(7)	(8)	(9)	(10)	(11)	(12)
SERVS	$3.6\mu\text{m} < 23.1$	5.0	$0.5''$	0.34	4701	1.0	3994	117	96.8%	4.2%	97.3%
VIDEO	$K_s < 23.8$	4.5	$0.3''$	0.24	4389	1.3	3804	104	86.3%	8.0%	94.4%
CFHTLS-wide	$i < 24.8$	5.4	$0.2''$	0.27	5197	1.5	4138	118	75.6%	15.6%	90.8%
HSC-SSP	$i < 26.5$	5.4	$0.1''$	0.13	5134	2.4	4192	114	78.6%	18.4%	87.3%
Summary	N/A	N/A	N/A	N/A	5247	5170	4913	23	93.1%	5.8%	97.1%

SERVS counterparts with  $MR > 0.9$ , suggesting that these secondary and tertiary counterparts are unlikely to be true counterparts of X-ray sources. For completeness, these secondary and tertiary counterparts are also reported in our final catalog in Table A.

For the remaining 316 sources, most of these sources have  $\text{DET\_ML} \geq 10.8$  in at least one band, and thus they are unlikely to be spurious detections. 234 of these 316 sources still have at least one OIR counterpart candidate within the  $r_{99\%}$  circle. Therefore, 5170 X-ray sources have at least one OIR counterpart candidates within  $r_{99\%}$ . Of the other 82 sources, 77 still have at least one OIR counterpart candidate within the  $10''$  counterpart-searching radius. We find 5 sources that are completely “isolated”, i.e., no counterpart candidates were found within a  $10''$  search radius. Visual inspection of these sources shows that all of the 5 sources coincide with a bright star, thus making the pipeline OIR photometry unreliable. Fig. 13 presents the positional offsets between the X-ray sources and the reliably matched sources. The small median positional offsets in RA and DEC directions demonstrate the quality of our astrometry, and the histograms of the positional offsets for sources binned in different  $\sigma_x$  show that our empirically-derived positional uncertainties are reliable. For each source, we also generate postage-stamp images in the X-ray, mid-IR, near-IR, and optical wavelengths. For illustration, we show a random collection of 16 X-ray sources with reliable counterparts in Figure 14.

## 5.2 Counterpart identification reliability

We assess the reliability of the *LR* matching results using the Monte Carlo simulation approach described in Broos et al. (2007) and Xue et al. (2011). Compared to the simple estimation based on matching OIR catalogs to a random X-ray catalog, the Broos et al. (2007) method usually provides a more realistic assessment of the matching reliability. As described in Broos et al. (2007) and Broos et al. (2011), we consider our X-ray sources to consist of two different intrinsic populations, the “associated population” and the “iso-

lated population”. The associated population is comprised of X-ray sources that do have a real counterpart in the corresponding OIR catalog, and the X-ray sources that should not have any OIR counterparts belong to the isolated population.

For the associated population, counterpart-matching procedures can produce three different outcomes: (1) an X-ray source is matched to its correct counterpart (correct match, or CM), (2) an X-ray source is matched to an incorrect counterpart (incorrect match, or IM), and (3) no counterparts were recovered (false negative, or FN). We define spurious fraction of the associated population is defined as  $N_{\text{IM}}/(N_{\text{IM}} + N_{\text{CM}})$ . For the isolated population, there are two possible matching results: (1) no counterparts are found (true negative, or TN), and (2) an OIR source is identified as a counterpart (false positive, or FP). The spurious fraction of the isolated population is defined as the number of false-positives divided by the size of the X-ray catalog. By definition, the spurious matches for these two populations are intrinsically different. The chance for the X-ray sources in the isolated population to have a counterpart is mostly determined by the source surface density of the OIR catalog being matched. On the other hand, since X-ray sources in the associated population must have a real OIR counterpart within a reasonable search radius, the spurious fraction is essentially determined by how well can the *LR* matching method discern a real counterpart from background sources.

In order to estimate the fractions of X-ray sources in both populations for our catalog, we simulate each population separately. The details of the simulation procedure can be found in the appendix of Broos et al. (2007) and §5 of Broos et al. (2011). A brief summary of the simulations: (1) For the “associated population”, we remove all OIR sources considered to be a match in §5.1, then move the position of each OIR source by  $1'$  in a random direction. We then generate fake OIR “counterparts” for each X-ray source in our catalog based on the X-ray and OIR positional uncertainties, and the expected magnitude distributions derived in §5.1. (2) For the “isolated population”, we create mock

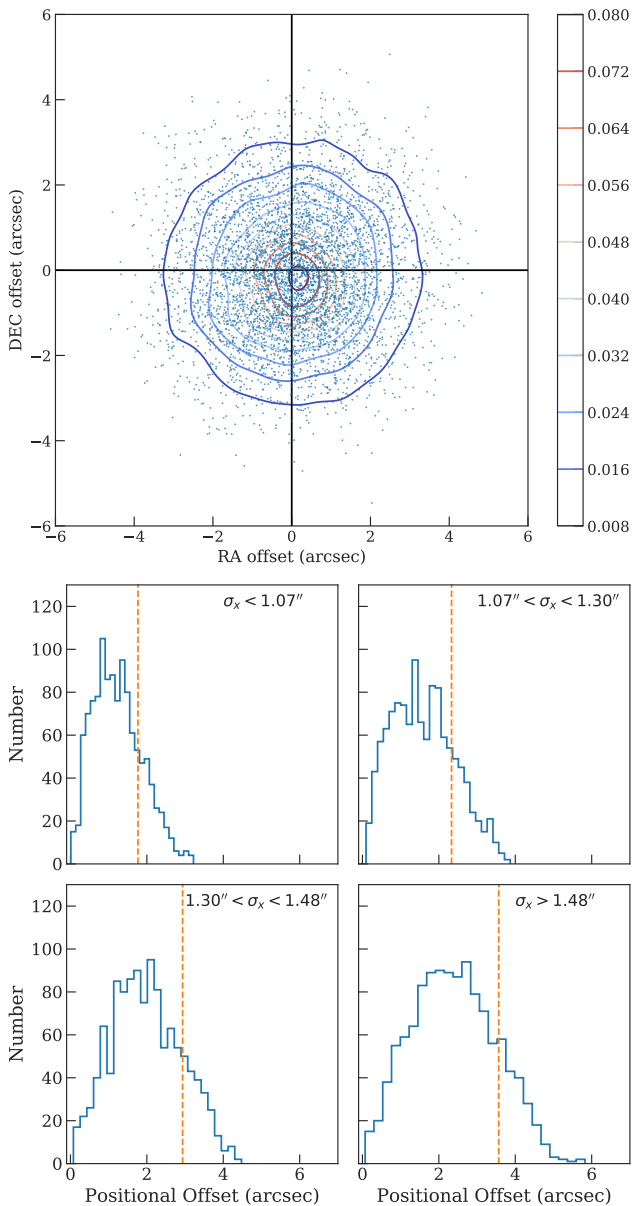


**Figure 13.** *Top:* Distribution of the positional offsets in the RA vs. DEC plane for the 4936 reliably matched sources. The contours represent the isodensity levels of the points. The median positional offsets are  $< 0.1''$  in both the RA and DEC directions (the red contour). *Bottom:* Histograms of positional offsets for the 4936 reliably matched sources, divided into four bins based on their positional uncertainties. In each panel, we also mark the median 68% positional offset value ( $r_{68\%}$ ) as the vertical dashed line.

X-ray sources that are at least  $20''$  away from any real X-ray sources.

A total of 100 simulations are carried out for each population, and we run the *LR* matching procedures on each simulation as described in §5.1. The simulations of the isolated populations usually produce a much higher spurious fraction (i.e., the number of false-positives divided by the size of the X-ray catalog). For the SERVS, VIDEO, CFHTLS, and HSC-SSP catalogs, the median spurious fractions of the

isolated populations are 19%, 24%, 30%, and 40%, respectively. For the associated populations, the spurious fractions (defined as  $N_{\text{IM}}/(N_{\text{IM}}+N_{\text{CM}})$ ) for SERVS, VIDEO, CFHTLS, and HSC-SSP are 3%, 5%, 7%, and 9%, respectively.

For the *LR* matching results with the real data, X-ray sources that were not reliably matched to any counterparts (with a total number of  $N_{\text{negative}}$ ) should contain a mixture of the FNs of the associated population and the TNs of the isolated population. Therefore, we can use the median FN and TN from simulations to estimate the fraction of X-ray sources in the associated population ( $f_{\text{AP}}$ ):

$$N_{\text{negative}} = N_{\text{FN}} \times f_{\text{AP}} + N_{\text{TN}} \times (1 - f_{\text{AP}}). \quad (9)$$

With  $f_{\text{AP}}$ , we can estimate the expected number of X-ray sources that have a spurious match as the weighted sum of the numbers of IM and FP. The false-matching rate,  $f_{\text{False}}$ , should therefore be:

$$f_{\text{False}} = (N_{\text{IM}} \times f_{\text{AP}} + N_{\text{FP}} \times (1 - f_{\text{AP}}))/(N_{\text{positive}}). \quad (10)$$

Here we consider  $N_{\text{positive}}$  as the combination of both the “reliable” and “acceptable” matches reported in Table 4. We carry out simulations for each OIR catalog. The values of  $f_{\text{False}}$  and  $f_{\text{AP}}$  for each OIR catalog are also reported in Table 4. Due to the high  $f_{\text{AP}}$  values, the false-matching rates of our matching results are mostly determined by the spurious fractions of the associated populations, which are much lower than those of the isolated populations. Notably, adopting the *Chandra*-matched counterpart magnitude density,  $q(m)_{\text{Chandra}}$ , does reduce the false-matching rates compared to those derived using  $q(m)_{\text{XMM-Newton}}$ . For the SERVS and VIDEO catalogs, the improvements are marginal ( $< 0.5\%$ ), while the improvements for CFHTLS and HSC-SSP are more significant ( $\approx 2\%$  and  $6\%$ , respectively).

We further scrutinize the *LR* matching reliabilities by making use of the 223 CSC sources and their multiwavelength matching results described in §5.1. We assess the reliability of the matching results of these *Chandra* sources using the aforementioned Monte Carlo method, and find that the false-match fractions are 0.9%, 1.4%, 2.8%, and 3.3%, for SERVS, VIDEO, CFHTLS, and HSC-SSP, respectively. For each catalog, we also directly compare the reliable matches obtained with *XMM-Newton* and *Chandra* positions. We find that 97%, 94%, 91%, and 87% of the reliable *Chandra* matching results and the reliable *XMM-Newton* results are the same for the SERVS, VIDEO, CFHTLS, and HSC catalogs, respectively. Note that the high “identical fraction” between the matching results obtained using *Chandra* positions and *XMM-Newton* positions are slightly lower than the false-matching rates calculated based on the Monte Carlo simulation because we only compare X-ray sources with reliable counterparts of the *Chandra* and *XMM-Newton* positions in each catalog. Similar to the full *XMM-Newton* catalog, we also select “primary” counterparts for the *Chandra* sources using the same priority orders. 85%, 10%, 1%, and 4% of the *Chandra* sources have their “primary” counterparts from SERVS, VIDEO, CFHTLS, and HSC-SSP, respectively. When comparing the primary counterparts of these *Chandra* sources and the primary counterparts of the corresponding *XMM-Newton* sources,  $\approx 97\%$  of them are

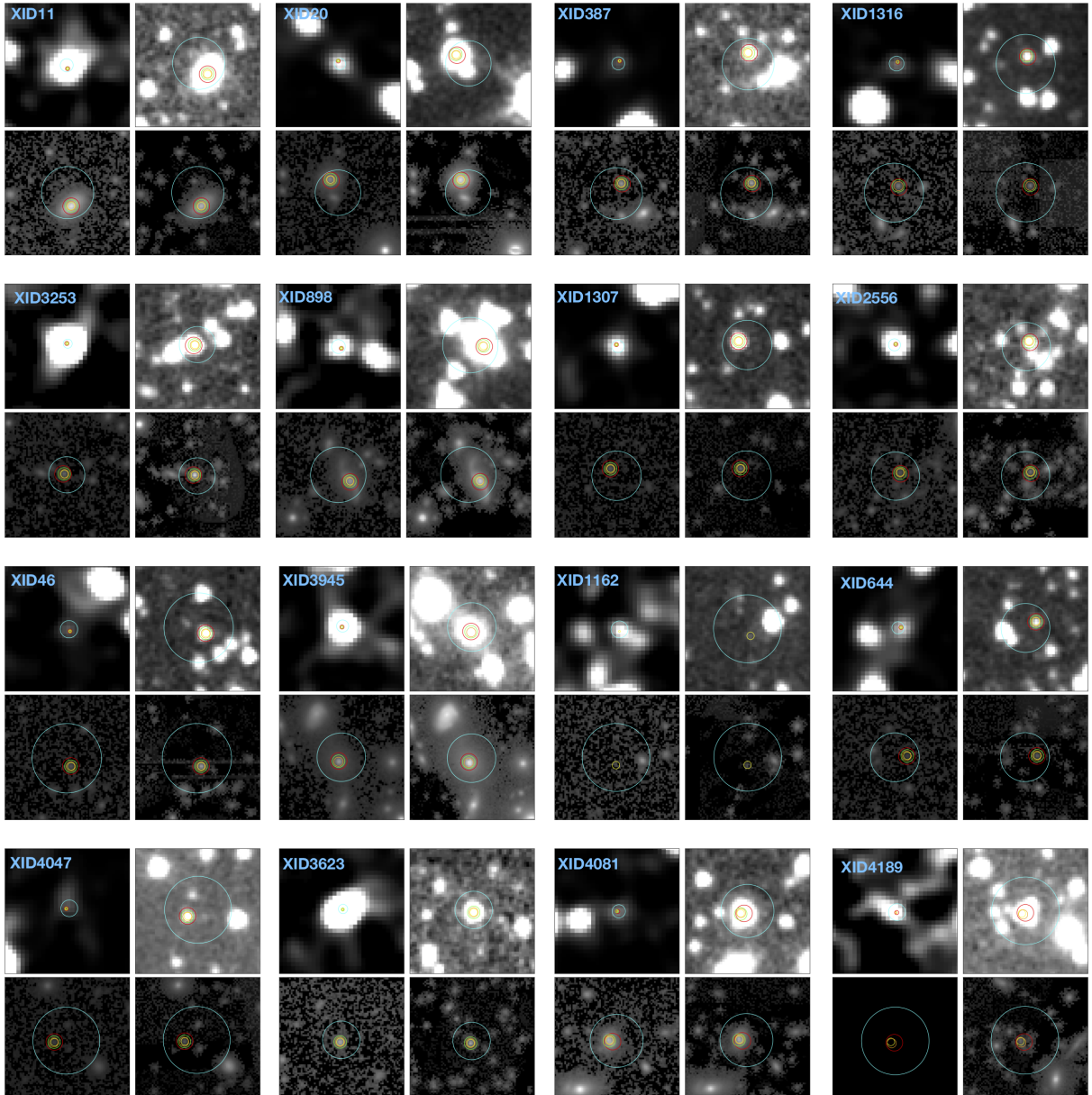


**Figure 14.** Postage-stamp images for 16 randomly selected X-ray sources in our catalog. For each source, we show (1) Full-band X-ray image (upper-left panel) with the unique source ID from Table A. (2)  $3.4\mu\text{m}$  mid-IR image from SERVS (upper-right panel) (3)  $Ks$ -band near-IR image from VIDEO (lower-left panel) (4)  $i$ -band optical image from HSC-SSP (lower-right panel). Due to the large pixel size, the X-ray image for each source is set at  $2' \times 2'$ . For the OIR images, the sizes are set at  $0.5' \times 0.5'$ . In each image, the X-ray position is marked as the cyan circle with the  $r_{99}$  radius. The position of the most-probable mid-IR SERVS counterpart is marked as the red circle with a  $2''$  radius. The positions of VIDEO, CFHTLS, and HSC-SSP counterparts are marked as  $1''$  circles of green, orange, and yellow circles with  $1.5'', 1.1'',$  and  $0.9''$ , respectively. The entire set of postage-stamp images is available in the electronic version.

identical, demonstrating that the matching results of the *XMM-Newton* catalog are highly reliable.

### 5.3 Spectroscopic redshifts

The XMM-LSS region is covered by a number of spectroscopic redshift surveys that target galaxies with various optical magnitude constraints: the PRImus Multi-Object Survey (PRIMUS; Coil et al. 2010), the VIMOS Public Extragalactic Redshift Survey (VIPERS; Garilli et al. 2014), the

VIMOS VLT Deep Survey (VVDS; Le Fevre et al. 2013). As part of the SDSS-BOSS program, 3042 X-ray sources found in the XXL-N field ( $25 \text{ deg}^2$ ) with  $r < 22.5$  were all followed-up by SDSS (Menzel et al. 2016). Also, there are three other redshift surveys in the XMM-LSS region that target near-IR selected galaxies, including the spectroscopic follow-up observations of the UKIDSS Ultra-Deep Survey (UDSz; Bradshaw et al. 2013; McLure et al. 2013), the 3D-HST Survey (Skelton et al. 2014; Momcheva et al. 2016) in the UDS region, and the Carnegie-Spitzer-IMACS Redshift

**Table 5.** Redshift catalogs used in this work. Column 1: Redshift survey name. Column 2: Survey instrument. Column 3: Survey sensitivity. Column 4: Targeting fields. Column 5: Survey area. Column 6: Total number of redshifts matched the main X-ray catalog. Column 7: Total number of redshifts assigned to the X-ray sources in the main catalog.

Catalog (1)	Instrument (2)	Survey sensitivity (3)	Targeting fields (4)	Area (5)	$N_{\text{matched}}$ (6)	$N_{\text{assigned}}$ (7)
3D-HST CSI	WFCS G141 Grism	$JH_{\text{IR}} \lesssim 24$	UDS	191.2 arcmin <sup>2</sup>	13	5
	IMACS (Uniform-Dispersion Prism)	[3.6 μm]AB $\lesssim 21$	XMM-LSS	6.9 deg <sup>2</sup>	300	57
PRIMUS	IMACS (Low-Dispersion Prism)	$i \lesssim 23.5$	XMM-LSS	2.9 deg <sup>2</sup>	763	364
	SDSS	$r \lesssim 22.5$	XXL-North	25 deg <sup>2</sup>	1104	1104
UDSz	BOSS	$K < 23$	UDS	0.5 deg <sup>2</sup>	24	17
VVDS	VIMOS/FORS2	$17.5 \lesssim i \lesssim 24.5$	XMDS+SXDS	3 deg <sup>2</sup>	87	43
VIPERS	VIMOS	$i \lesssim 22.5$	XMM-LSS	7.8 deg <sup>2</sup>	350	172

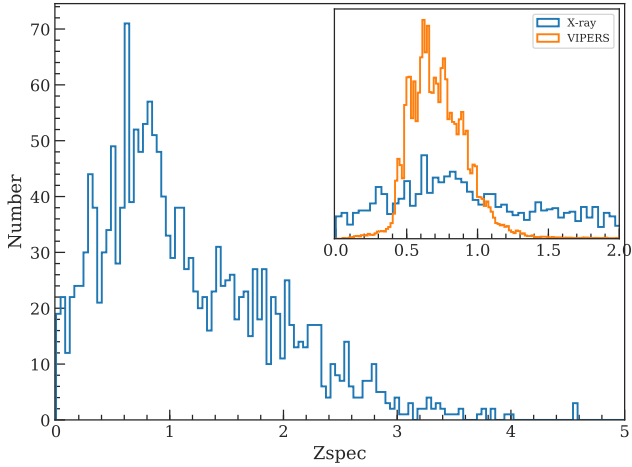


**Figure 15.** Distribution of the redshifts in bins of  $\Delta z = 0.04$  for the 1762 X-ray sources with spectroscopic redshift measurements from the literature. The redshift spikes are likely associated with X-ray large-scale structures (e.g., Luo et al. 2017). A comparison between the normalized redshift distribution of the X-ray sources and that of the galaxies from the VIPERS survey is also shown in the insert, which suggests that some of the redshift spikes (e.g.,  $z \approx 0.6$ ) of X-ray sources overlap with those of the general galaxy population.

Survey (CSI; Kelson et al. 2014). We list the properties of each redshift catalog in Table 5.

We adopt the same nearest-neighbor matching criterion with a 1'' matching radius to associate these redshifts to each OIR catalog. The redshift for each X-ray source is determined by the coordinates of its primary OIR counterpart. In cases where redshifts from different catalogs do not agree with each other, we choose redshifts using the following ordering (ranked by spectral resolution): SDSS, VVDS, VIPERS, UDSz, PRIMUS (reliable), CSI (reliable), 3D-HST, PRIMUS (acceptable), CSI (acceptable). Of the 5252 sources in our main X-ray source catalog, 1762 of them have spectroscopic redshifts ranging from  $0.002 < z < 4.57$ . We also show the redshift histogram in Fig. 15 in bins of  $z = 0.04$ . Note that there are several redshift spikes indicative of X-ray large-scale structures (e.g., Luo et al. 2017). Notably, the X-ray source redshift spike at  $0.6 < z < 0.7$  appears to coincide with one of the major large-scale structures seen in the VIPERS redshift survey (see Fig. 14 of Garilli

et al. 2014 and the insert panel of Fig. 15). The cumulative histogram of the  $i$ -band magnitudes of the sources with redshifts are shown in the left panel of Fig. 16.

#### 5.4 Photometric redshifts

We note that high-quality photometric redshifts for AGNs are not yet available for our survey region, but are already being constructed for the general galaxy populations. In particular, in a  $\approx 1$  deg<sup>2</sup> area within the XMM-LSS region, Nyland et al. (2017, N17 hereafter) have presented a “forced-photometry” catalog which is well-suited for photometric redshift measurements<sup>21</sup>. We make use of the 12-band photometry from  $u'$  to IRAC 4.5μm (from CFHTLS, VIDEO, and SERVS) in N17 to derive photometric redshifts for the X-ray sources in this region using the methods described in Yang et al. (2014). We match the N17 catalog to the coordinates of the primary counterparts of the 966 X-ray sources in our source catalog that have reliable counterparts in VIDEO,<sup>22</sup> and found 936 matches using a 1'' matching radius. We exclude 177 X-ray sources that are classified as broad-line AGNs according to their optical spectra due to their much higher photometric redshift uncertainties. Since the flux uncertainties in N17 do not account for uncertainties in PSF modeling, we adopt an additional 3% to the flux errors, which is typical of PSF modeling uncertainties (e.g., §5.3 of Yang et al. 2014).

Following the recipe of Yang et al. (2014), we measure the photometric redshifts using the SED-fitting code EAZY (Brammer et al. 2008) using the default galaxy templates and settings, and an additional obscured AGN template from Polletta et al. (2007). As described in §5.6 of Yang et al. (2014), we perform iterative procedures to adjust the photometric zero points; the zero-point corrections are  $\lesssim 0.1$  mag. For each source, EAZY calculates a parameter  $Q_z$  (see Eq. 8 of Brammer et al. 2008) to indicate photometric-redshift quality. We consider photometric redshifts with  $Q_z < 1$  as reliable (see §6.3 of Yang et al. 2014). There are 92 sources with  $Q_z < 1$  and reliable spectroscopic redshifts, which can be used to assess the quality of photometric-redshift measurements. The normalized median

<sup>21</sup> The photometric redshifts reported in N17 are not yet publicly available

<sup>22</sup> The N17 catalog is based on the forced-photometry on the positions of the sources with VIDEO detections.

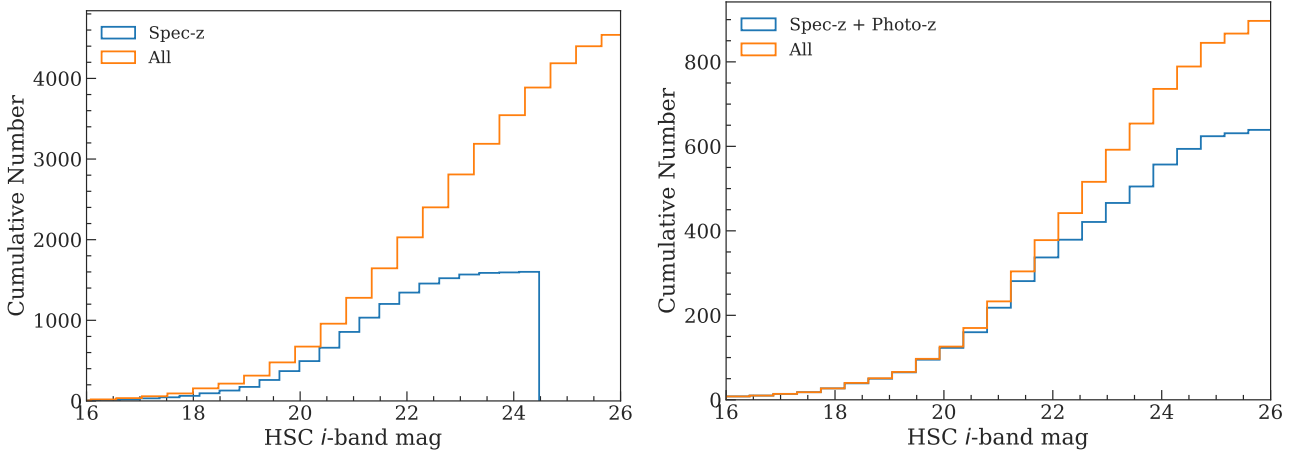


**Figure 16.** *Left* – Cumulative distribution of the HSC  $i$ -band magnitudes for the X-ray sources with spectroscopic redshifts is indicated by the blue histogram. The cumulative  $i$ -band magnitude distribution for the full X-ray catalog is shown as the orange histogram. *Right* – Similar to the figure in the left, but only for the 1 deg<sup>2</sup> subfield in our survey that has publicly available forced-photometry for photometric redshift measurements. The blue histogram is the cumulative distribution of the X-ray sources with spectroscopic or high-quality photometric redshifts; and the orange histogram shows the cumulative distribution of all X-ray sources in the 1 deg<sup>2</sup> region.

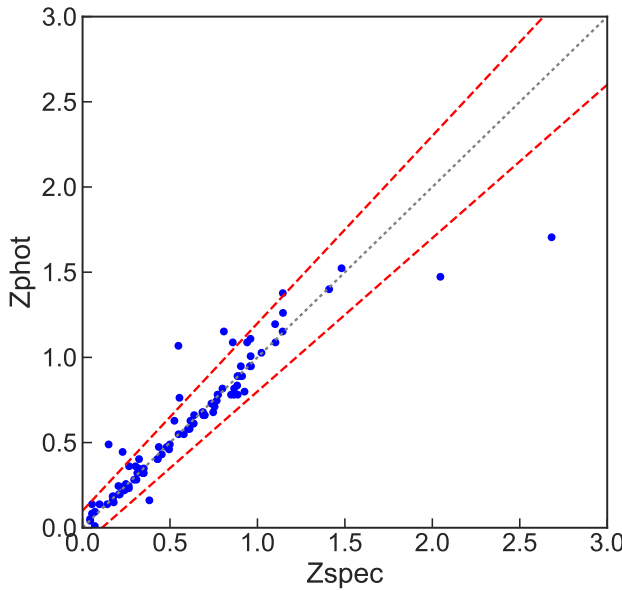


**Figure 17.** Spectroscopic and photometric redshifts for the 92 non-broad-line AGN sources with high quality photometric redshifts and spectroscopic redshifts. The red dashed lines mark the  $|\Delta z| / (1 + z_{\text{spec}}) = 0.15$  thresholds for outliers, and the black dotted line marks the  $Z_{\text{spec}} = Z_{\text{phot}}$  relation.

absolute deviation (NMAD) is  $\sigma_{\text{NMAD}} = 0.024$ , with an outlier (defined as  $|\Delta z| / (1 + z_{\text{spec}} > 0.15)$ ) fraction of 7.7%, which is comparable to the photometric redshift reliability reported in Yang et al. (2014) for CDF-N. Fig. 17 compares the photometric and spectroscopic redshifts for these 92 sources. The 1 deg<sup>2</sup> area covered by N17 contains 388 reliable photometric redshifts for sources that do not have spectroscopic redshift measurements, increasing the fraction of sources with redshifts from  $\approx 32\%$  to  $\approx 72\%$ . A similar forced-photometry catalog for our full survey region, including the deep HSC-

SSP photometry is currently being constructed (Pforr et al., in preparation); we expect to achieve at least 70% photometric+spectroscopic redshift completeness for our full X-ray catalog when the full forced-photometry catalog becomes available.

## 5.5 Source properties and classification

In this section we briefly discuss some of the properties of the 4936 sources with robust or acceptable counterparts. For the X-ray sources with secure redshifts, we calculate their rest-frame 2–10 keV “apparent” luminosity assuming a  $\Gamma = 1.7$  power-law spectrum corrected for Galactic absorption. In Fig. 18, we compare the flux, redshift, and luminosity distributions of our sample to those from archival X-ray surveys, including XMM-COSMOS, COSMOS-Legacy, and Stripe 82X. The comparisons in the middle and right panels are limited to sources with available spectroscopic redshifts in the Stripe-82 and XMM-LSS regions. The right panel of Fig. 18 demonstrates that our catalog occupies a valuable part of parameter space among X-ray surveys by more than doubling the source counts of the XMM-COSMOS survey, which will enable a wide range of science that was previously limited by either survey sensitivity or cosmic variance.

We also include basic source classifications in our catalog. For sources with spectroscopic observations, we directly make use of the spectroscopic classifications when available. A total of 833 sources are classified as AGNs based on the broad-line spectroscopic flags specified in SDSS, VIPERS, or VVDS catalogs. For the other sources, we use the criteria described in Luo et al. (2017) to select AGN: (1) An X-ray luminosity threshold where we regard sources with rest-frame  $L_{2-10 \text{ keV}} > 3 \times 10^{42} \text{ erg s}^{-1}$  as an AGN. A total of 1504 sources satisfy this criterion. (2) X-ray bright sources with X-ray-to-optical or X-ray-to-near-IR flux ratios larger than  $\log f_x/f_R > -1$  or  $\log f_x/f_{Ks} > -1.2$ , respectively. There are 3409 sources with  $\log f_x/f_R > -1$  and 4071 sources with  $\log f_x/f_{Ks} > -1.2$ , totaling 4479 sources can be classified as an AGN based on their  $f_x/f_R$  or  $f_x/f_{Ks}$  values. We show the

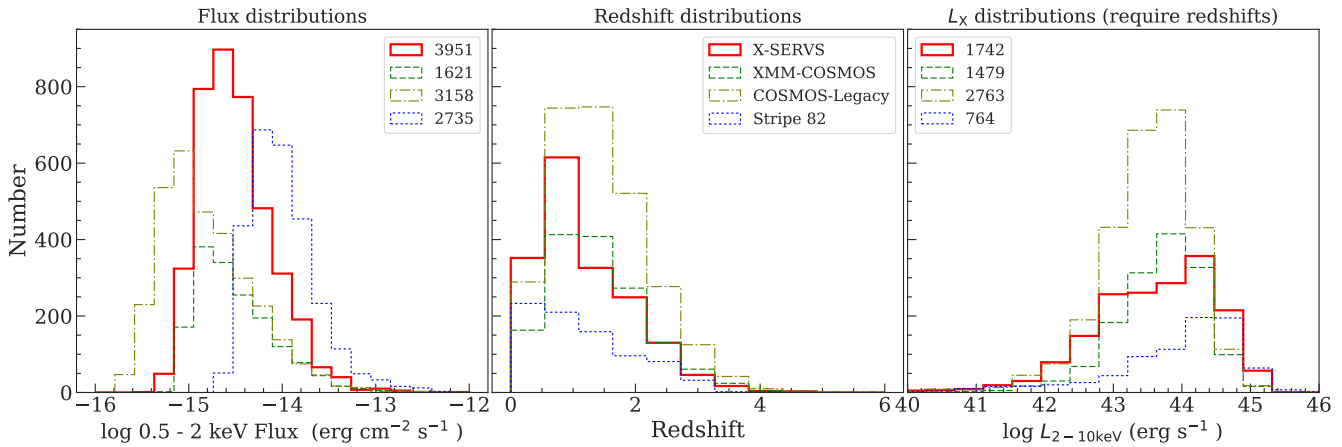


**Figure 18.** A comparison between this work (solid red line), XMM-COSMOS (green dashed line), COSMOS-Legacy (brown dash-dotted line), and Stripe 82-X (blue dotted line). Distributions shown in panels from left to right are: 0.5–2 keV flux, redshift, and  $\log L_{2-10 \text{ keV}}$ , respectively. The left panel shows the distribution of soft-band fluxes for the soft-band detected sources in each catalog, no redshift information is required. The numbers of the soft-band sources are shown in the left panel. For the middle and right panels, the histograms are for the same set of sources with redshift measurements, with source numbers marked in the right panel.

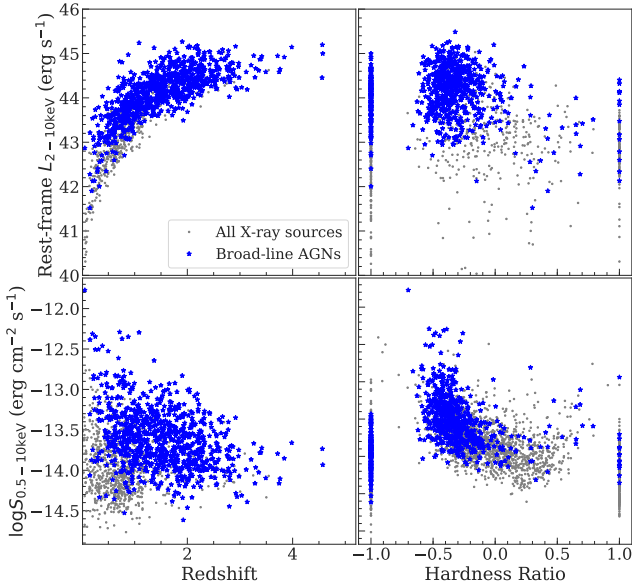


**Figure 19.** Properties of the 1762 X-ray sources with spectroscopic-redshift measurements, including (1) the  $L_{2-10 \text{ keV}}$  vs.  $z$  distribution (top-left), (2)  $L_{2-10 \text{ keV}}$  vs. hardness ratio (top-right), (3) 0.5–10 keV flux vs. redshift (bottom-left), (4) 0.5–10 keV flux vs. hardness ratio (bottom-right). Broad-line AGNs are marked as the blue stars.

$L_X - z$  distribution of our sample in Fig. 19, along with the  $L_X$  vs. HR, HR vs. full-band flux, and full-band flux vs. redshift distributions. We also show the flux-ratio distributions in Fig. 20. The total number of sources classified as AGNs is 4702, or  $\approx 89\%$  of the total sample. For the sources not classified as an AGN, 118 of them have spectroscopic redshift measurements, including 10 stars with  $z \leq 0$ , and 108 sources low X-ray luminosity sources. Given their relatively weak X-ray to OIR ratios, they are likely powered by star-formation

processes in galaxies given their relatively weak X-ray to OIR ratios and low X-ray luminosities. For the remaining 432 sources, we expect many of them will be identified as X-ray AGNs when redshift information becomes available. Since most of the lower-redshift galaxies already have spectroscopic redshifts from existing wide-field redshift surveys in XMM-LSS, the remaining unclassified sources are likely to lie at higher redshifts. For instance, an X-ray source with the median X-ray flux of the 432 unclassified sources will have  $L_X > 3 \times 10^{42} \text{ erg s}^{-1}$  at  $z \geq 0.3$ .

## 6 SUMMARY

In this work, we present a new X-ray point-source catalog in the XMM-LSS region constructed using both considerable new AO-15 and archival *XMM-Newton* data. The main results are the following:

1. Our X-ray catalog is constructed based on data in a  $5.3 \text{ deg}^2$  rectangular region centered at RA= $35.58^\circ$ , DEC= $-4.965^\circ$ . A total of 155 pointings from 149 different *XMM-Newton* ObsIDs are used, with a total of 2.7 Ms background-filtered exposure time (1.1 Ms from AO-15). The median value of the cleaned PN exposure time is 46 ks for the full  $5.3 \text{ deg}^2$  field, reaching the desired uniformity and survey depth (see §2).
2. The main X-ray source catalog is generated using EWAVELET and EMLDETECT. We list all 5252 sources with EMLDETECT DET\_ML  $> 6$  in the soft-band (0.5–2 keV), hard-band (2–10 keV), or full-band (0.5–10 keV). Of the 5252 sources, we find 2866 of them to be the same X-ray sources identified in previous X-ray surveys in our survey area (e.g., the XMM-XXL-North survey; Liu et al. 2016), and 2386 are newly discovered X-ray sources (see §3.4).
3. The median fluxes in  $\text{erg cm}^{-2} \text{ s}^{-1}$  for the three X-ray bands are  $2.9 \times 10^{-15}$  (0.5–2 keV),  $1.5 \times 10^{-14}$  (2–10 keV), and  $9.4 \times 10^{-15}$  (0.5–10 keV). There are 2928 sources with more than

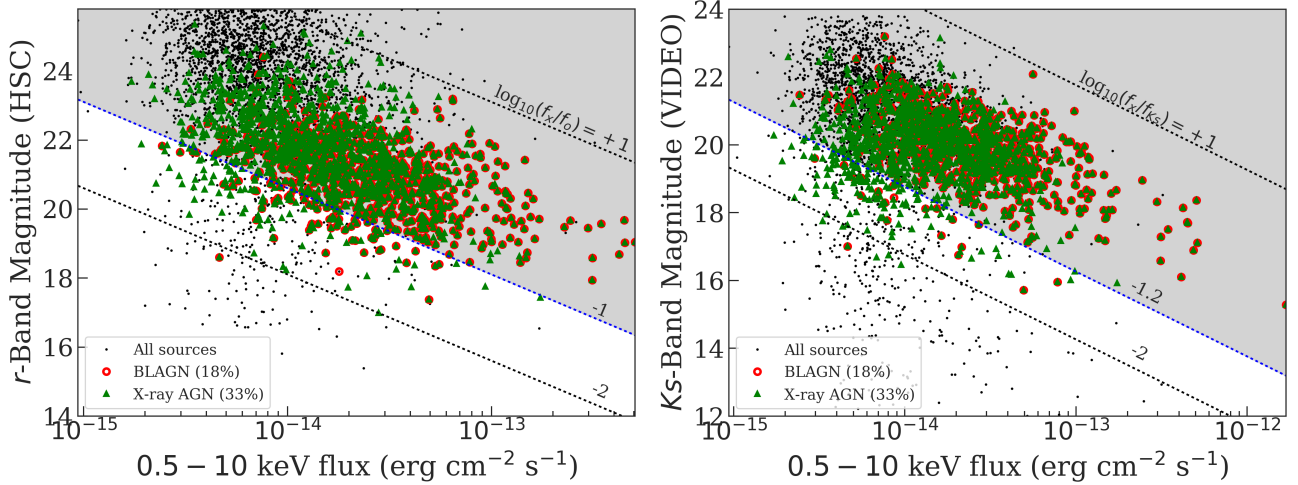


**Figure 20.** Left – Distributions of the full-band (0.5–10 keV) X-ray flux and the optical flux in the  $r$ -band. Right – Full-band X-ray flux versus the near-IR flux in the  $Ks$ -band. In both plots, the shaded regions mark the “AGN” regime as defined by the  $\log_{10} f_X/f_o > -1$  (left) or the  $\log_{10} f_X/f_{Ks} > -1.2$  (right) thresholds as described in §4.4 of Xue et al. (2011). For sources with spectroscopic redshift measurements, we also mark those with  $L_X > 3 \times 10^{42}$  erg s<sup>-1</sup> as the green triangles. The 833 sources with optical spectra consistent with broad-line AGNs are also marked as open red circles.

100 X-ray counts in full-band (PN + MOS), and 126 sources with more than 1000 X-ray counts (see §3.4).

4. Monte Carlo simulations indicate that the number of spurious sources should be  $\approx 41$  with a DET\_ML= 6.0 threshold, corresponding to  $\approx 99.2\%$  reliability. If we raise the detection threshold to DET\_ML= 10.8, or 99.8% reliability, the expected number of spurious sources would be  $\approx 12$  (§4).
5. The absolute astrometry of the *XMM-Newton* catalog is registered to the WCS frame of the Subaru HSC-SSP survey (§3.1). The positional uncertainties for the X-ray sources are determined based on an empirical relation between the X-ray-to-optical positional offsets and the X-ray source counts. Our empirical positional uncertainties are well-characterized by the Rayleigh distribution. The median positional uncertainties in the soft, hard, and full-bands are: 1.31'', 1.35'', and 1.37'', respectively (see §3.3).
6. We search for OIR counterparts in the SERVS, VIDEO, CFHTLS, and HSC-SSP surveys, and we find that 98% (5170/5252) of the X-ray sources have at least one OIR counterpart candidates within the 99.73% positional uncertainties ( $r_{99\%}$ ). We also find that  $\approx 94\%$  (4936/5252) of the X-ray sources have at least one reliable OIR counterpart (§5.1). We collect 1762 secure redshifts from SDSS, VIPERS, VVDS, UDSz, PRIMUS, CSI, and 3D-HST (§5.3). For a 1 deg<sup>2</sup> subfield in our survey region, we make use of the forced-photometry catalog from N17 to compute photometric redshifts (§5.4). We find that we can achieve  $> 70\%$  spectroscopic+photometric redshift completeness in the 1 deg<sup>2</sup> subfield. We expect to expand the photometric redshift measurements to all of our X-ray sources when the forced-photometry catalog for the full XMM-LSS field is released.
7. We test the matching results using a subsample of 223 X-ray sources with a reliable *Chandra* counterpart from CSC 2.0. We find that  $\approx 97\%$  of the matching results from *XMM-Newton* and *Chandra* are identical, demonstrating our multiwavelength matching results are highly reliable (see §5.2).
8. We classify 4706 X-ray sources as AGNs. The classification

is based on their optical spectra from SDSS, VIPERS, or VVDS (833); X-ray luminosity larger than  $3 \times 10^{42}$  erg s<sup>-1</sup> (1574); and large X-ray-to-optical and X-ray-to-NIR flux ratios (4589). See §5.5 for details.

The X-ray source catalog presented in this work is the first  $> 2$  deg<sup>2</sup> X-ray survey with sensitivity comparable to that of COSMOS. The 5.3 deg<sup>2</sup> wide-area and 46 ks depth survey will enable a wide range of studies. For instance, the large AGN sample and the excellent multiwavelength coverage will provide a means to exploring the behavior of AGNs in the multidimensional space of galaxy parameters. The wide-area of this survey will also enable studies of AGN triggering mechanisms as a function of environment. In the near future, the combination of AGN samples from this work, COSMOS, and additional X-ray surveys in other X-SERVS fields will sample the full range of cosmic large-scale structures, alleviating the cosmic variance uncertainties seen in previous COSMOS results (e.g., Meneux et al. 2009; de la Torre et al. 2010; Skibba et al. 2014), and advancing our understanding of the coevolution of SMBHs and their host galaxies.

## ACKNOWLEDGMENTS

We acknowledge the support of NASA grant NNX17AF07G (CTJC, WNB). FEB acknowledges support from CONICYT-Chile (Basal-CATA PFB-06/2007, FONDECYT Regular 1141218), the Ministry of Economy, Development, and Tourism’s Millennium Science Initiative through grant IC120009, awarded to The Millennium Institute of Astrophysics, MAS. MJJ was supported by the Oxford Centre for Astrophysical Surveys, which is funded through generous support from the Hintze Family Charitable Foundation. MJJ and BH acknowledge support from the UK Science and Technology Facilities Council [ST/N000919/1]. YQX was supported by NSFC-11473026, NSFC-11421303,

and the CAS Frontier Science Key Research Program (QYZDJ-SSW-SLH006).

## APPENDIX A: MAIN CATALOG DESCRIPTION

Here we describe the columns of the main X-ray source catalog, Table A. Throughout the table, we mark null values as  $-99$ .

### X-ray properties

Columns 1–100 give the X-ray properties of our sources. Columns for the soft-band results are marked with the “SB\_” prefix. Columns for the hard and full band results are marked with the “HB\_” and “FB\_” prefixes, respectively. Note that we have calculated the upper limits of counts, count rates, and fluxes for the non-detections (Eq. 3). For these upper limits, their corresponding uncertainty columns are set as  $-99$ .

- (1) Column 1: The unique source ID (XID) assigned to each X-ray source.
- (2) Columns 2–3: RA and DEC in degrees of the X-ray source. The positions are determined based on EMLDETECT. Based on availability, we use the positions from, in priority order, full-band, soft-band, and hard-band as the primary position of the X-ray source. Band-specific positions are listed in Columns 8–13.
- (3) Column 4: X-ray positional uncertainty ( $\sigma_x$ ) in arcsec based on the empirical relation between source counts and positional offsets to the HSC-SSP catalog. Note that this is not the  $\sigma$  of a 2D-Gaussian distribution but rather the scaling parameter of the univariate Rayleigh distribution (see §3.3 and Pineau et al. 2017 for details). The positional uncertainties are based on those of the full-band. For sources without a full-band detection, the soft or hard-band positional uncertainties are listed. See §3.3 for details.
- (4) Columns 5–6: 68% and 99.73% X-ray positional uncertainties in arcsec based on the Rayleigh distribution; see §3.3 for details.
- (5) Column 7: Positional uncertainties calculated by EMLDETECT,  $\sigma_{\text{eml}}$  in arcsec. Similar to  $\sigma_x$ , we list the full-band values when possible and list soft or hard-band  $\sigma_{\text{eml}}$  for sources not detected in the full band.
- (6) Columns 8–13: RA and DEC in degrees of the source in the soft, hard, and full bands, respectively.
- (7) Columns 14–16: The source-detection threshold in each band, DET\_ML, which is computed using EMLDETECT.
- (8) Columns 17–19: Total (PN + MOS1 + MOS2) exposure time in seconds in each band.
- (9) Columns 20–28: PN, MOS1, and MOS2 exposure time in seconds in each band.
- (10) Columns 29–31: Total background-map values (PN + MOS1 + MOS2) in counts per pixel in each band.
- (11) Columns 32–40: PN, MOS1, and MOS2 background-map values in counts per pixel in each band.
- (12) Columns 41–43: Total (PN + MOS1 + MOS2) net counts in each band.
- (13) Columns 44–52: PN, MOS1, and MOS2 net counts in each band.
- (14) Columns 53–64: Uncertainties of total, PN, MOS1, and MOS2 net counts in each band.

- (15) Columns 65–76: Total, PN, MOS1, and MOS2 net count rates in each band, in count s $^{-1}$ .
- (16) Columns 77–88: Uncertainties of total, PN, MOS1, and MOS2 net count rates in each band, in count s $^{-1}$ .
- (17) Columns 89–94: Flux and flux uncertainty in each bands, in erg cm $^{-2}$  s $^{-1}$ . The conversion factors between count rates and fluxes are derived assuming a power-law spectrum with a  $\Gamma = 1.7$  photon index and Galactic absorption column density for each EPIC detector. Note that no correction is made for possible intrinsic absorption. See §3.4 for details. The fluxes and uncertainties reported here are the error-weighted average of all EPIC detectors.
- (18) Columns 95–97: Hardness ratio, defined as  $(H - S)/(H + S)$ , where  $H$  is the total (PN + MOS1 + MOS2) net counts divided by total exposure time in the hard band and  $S$  is the total net counts divided by total exposure time in the soft band. The uncertainties on the HRs are calculated based on the count uncertainties using the error propagation method described in §1.7.3 of Lyons (1991). Sources detected only in the full-band are set to  $-99$  in all three columns. We note that one of the CCDs on MOS1 was affected by a micrometeorite impact, therefore  $H$  and  $S$  are sometimes calculated based on only results from two cameras with non-zero exposure time.
- (19) Columns 98: Rest-frame, “apparent” 2–10 keV X-ray luminosity (only corrected for Galactic absorption) computed as in §5.5.
- (20) Columns 99: CSC 2.0 source name of the nearest *Chandra* source in the CSC.
- (21) Columns 100: XXL-North catalog source name of the nearest *XMM-Newton* source in Liu et al. (2016).

### Multiwavelength matching results

Columns 101–112 show the multiwavelength matching results based on the  $LR$  method described in §5.1. In these columns, the 99.73% positional-uncertainty radius represents the quadratic sum of the positional uncertainties of each X-ray source and the corresponding OIR catalog (see Table 4).

- (1) Columns 101–104: Number of “counterpart candidates” from each OIR catalog within the 99.73% positional-uncertainty radius of each X-ray source. The average values of these columns are listed in Column (7) of Table 4.
- (2) Columns 105–108: Number of sources from each OIR catalog that satisfies  $LR \geq LR_{\text{th}}$ .
- (3) Column 109: Flag set to 1 if the X-ray source has at least one reliable counterpart with  $LR > LR_{\text{threshold}}$  from any of the four OIR catalogs. See §5.1 for details.
- (4) Column 110: Flag set to 1 if the X-ray source has no reliable counterparts, but has at least one acceptable counterpart from any of the four OIR catalogs. See §5.1 for details.
- (5) Column 111: Flag set to 1 if the X-ray source has no reliable or acceptable counterparts, but still has at least one counterpart candidate from any of the four OIR catalogs (i.e., is not an isolated X-ray source).
- (6) Column 112: Flag set to 1 if the X-ray source has no counterparts from any of the four OIR catalogs within the 99.73% positional-uncertainty radius.

### Multiwavelength properties

Columns 113–185 give the multiwavelength properties from each OIR catalog for the primary counterparts matched to X-ray sources using the *LR* method. Properties from SERVS, SWIRE, VIDEO, CFHTLS, and HSC-SSP are marked with prefixes “SERVS\_”, “SWIRE\_”, “VIDEO\_”, “CFHT\_”, and “HSC\_”, respectively.

- (1) Column 113: Catalog from which the primary counterpart is selected. The primary counterpart is chosen in priority order from SERVS, VIDEO, CFHTLS, and HSC-SSP, which is based on the matching reliability of each OIR catalog. See §5.2 for details.
- (2) Column 114–116: RA and DEC in degrees of the primary counterpart and its separation in arcsec from the X-ray source.
- (3) Column 117: The matching likelihood ratio (*LR*) of the primary counterpart.
- (4) Column 118: The matching reliability (*MR*) of the primary counterpart.
- (5) Columns 119–130: RA, DEC, and Object ID of the primary counterpart culled from the original OIR catalogs.
- (6) Columns 131–134: SERVS 1.9'' aperture photometry and the associated uncertainties in the 3.6 $\mu\text{m}$  and 4.5 $\mu\text{m}$  bands.
- (7) Columns 135–142: SWIRE 1.9'' aperture photometry and the associated uncertainties in the 3.6 $\mu\text{m}$ , 4.5 $\mu\text{m}$ , 5.8 $\mu\text{m}$ , and 8.0 $\mu\text{m}$ .
- (8) Columns 143–144: SWIRE 1.9'' aperture photometry and the associated uncertainties in the 24 $\mu\text{m}$  band.
- (9) Columns 145–154: VIDEO PSF photometry and uncertainties in AB magnitude in the *Z*, *Y*, *J*, *H*, and *Ks* bands.
- (10) Columns 155–164: CFHTLS PSF photometry and uncertainties in AB magnitude in the *u*, *g*, *r*, *i*, and *z* bands.
- (11) Columns 165–174: HSC CModel photometry and uncertainties in AB magnitude in the *g*, *r*, *i*, *z*, and *y* bands.
- (12) Columns 175–177: RA, DEC, and Object ID from the original redshift catalogs for the primary counterparts.
- (13) Column 178: Spectroscopic redshift adopted for the X-ray source. The redshifts are chosen based on the spectral resolution of the observations. See §5.3 for details.
- (14) Column 179: The catalog from which the redshift is culled from.
- (15) Column 180: Original redshift flag from one of the redshift catalogs. For SDSS, see <http://www.sdss.org/dr14/algorithms/bitmasks/#ZWARNING> for the definition of flags. For VVDS, see §3.4 of Le Fevre et al. (2013) for the definition of flags. For VIPERS, see §4.3 of Garilli et al. (2014) for the definition of flags. For PRIMUS, see <http://primus.ucsd.edu/version1.html#ztags> for the definition of flags. For CSI, see §4.6 of Kelson et al. (2014) for the definition of flags. For UDSz, see McLure et al. (2013) for the definition of flags. For the 3D-HST catalog, we only select redshifts with  $\sigma_z/(1+z) \leq 0.003$  and thus no redshift flags are included.
- (16) Column 181–184: Photometric redshift, the associated upper and lower uncertainties, and the photometric redshift quality parameter ( $Q_z$ ). See §5.4. The photometric-redshift measurements are limited to the 1 deg<sup>2</sup> area with forced-photometry from Nyland et al. (2017). See §5.3 for details.
- (17) Column 185: Flag set to 1 if the X-ray source is classified as an AGN based the “broad-line” flag in the original redshift catalog. Flag set to 2 if the X-ray source is classified as an AGN based on its X-ray luminosity, where  $L_X > 3 \times 10^{42}$  erg s<sup>-1</sup>. Flag set to 3 if the X-ray source is

classified as an AGN based on the large X-ray-to-optical or X-ray-to-near-IR flux ratios, see Fig. 20. Flag set to 0 if the source is not classified as an AGN. See §5.5 for details.

#### *Multiwavelength properties for additional counterparts*

In our source catalog, there are 947 X-ray sources with two  $LR \geq LR_{\text{th}}$  counterparts where the second-highest *LR* counterpart also satisfies  $LR \geq 0.5LR_{\text{primary}}$ . The highest *LR* counterparts are considered as “primary” with properties reported in Columns 113–180. Here we report the multiwavelength properties of the “secondary” counterparts in Columns 186–252, which are identical as Columns 113–180 except for the additional “SECONDARY\_” prefixes. There are also 20 X-ray sources with three  $LR \geq LR_{\text{th}}$  counterparts, where the secondary and the tertiary counterparts both satisfy the  $LR \geq 0.5LR_{\text{primary}}$  criterion. The multiwavelength properties of the secondary counterparts for these 20 sources are also reported in Columns 186–252. The properties for the tertiary counterparts are reported in Columns 253–319, which are identical as Columns 113–180 except for the additional “TERTIARY\_” prefixes.

## APPENDIX B: SUPPLEMENTARY MULTIWAVELENGTH MATCHING RESULTS WITH THE NWAY BAYESIAN CATALOG MATCHING METHOD

We supplement the *LR* matching results with the Bayesian catalog matching tool NWAY (Salvato et al. 2017).<sup>23</sup> The fundamental difference between the Bayesian approach and the likelihood-ratio approach is that the Bayesian approach makes use of the distance and magnitude priors from multiple catalogs simultaneously to select the most-probable counterpart in all catalogs considered. The details of NWAY’s matching methodology are described in Appendix B of Salvato et al. (2017).

NWAY computes three informative quantities for deciding the most-probable match, *p\_single*, *p\_any* and *p\_i*, where each possible counterpart has a different *p\_single* value based on its distance from the *XMM-Newton* position. This value could be weighted by the priors supplied (e.g., *q(m)* and *n(m)* in Eq. 6 are similar to a magnitude prior). In our case, *p\_single* is the posterior probability for a counterpart to be correctly associated with the X-ray source based on the angular separation from the X-ray position weighted by the magnitude-distribution prior, and the surface densities of the X-ray and OIR catalogs. For each X-ray source, *p\_single* of all possible counterparts is considered to compute a single *p\_any* value, which stands for the posterior probability of the X-ray source having any correct counterparts (i.e., *p\_any* = 0 if there are no OIR counterparts within the search radius of the X-ray source.) The last quantity, *p\_i*, is the relative probability of a possible counterpart being the correct match. For an X-ray source with multiple possible counterparts, the counterpart with the highest *p\_i* (*p\_i* (Best)) is considered to be the most-probable match and is assigned the MATCH\_FLAG = 1 flag by NWAY. Counterparts with *p\_i*

<sup>23</sup> <https://github.com/JohannesBuchner/nway>.

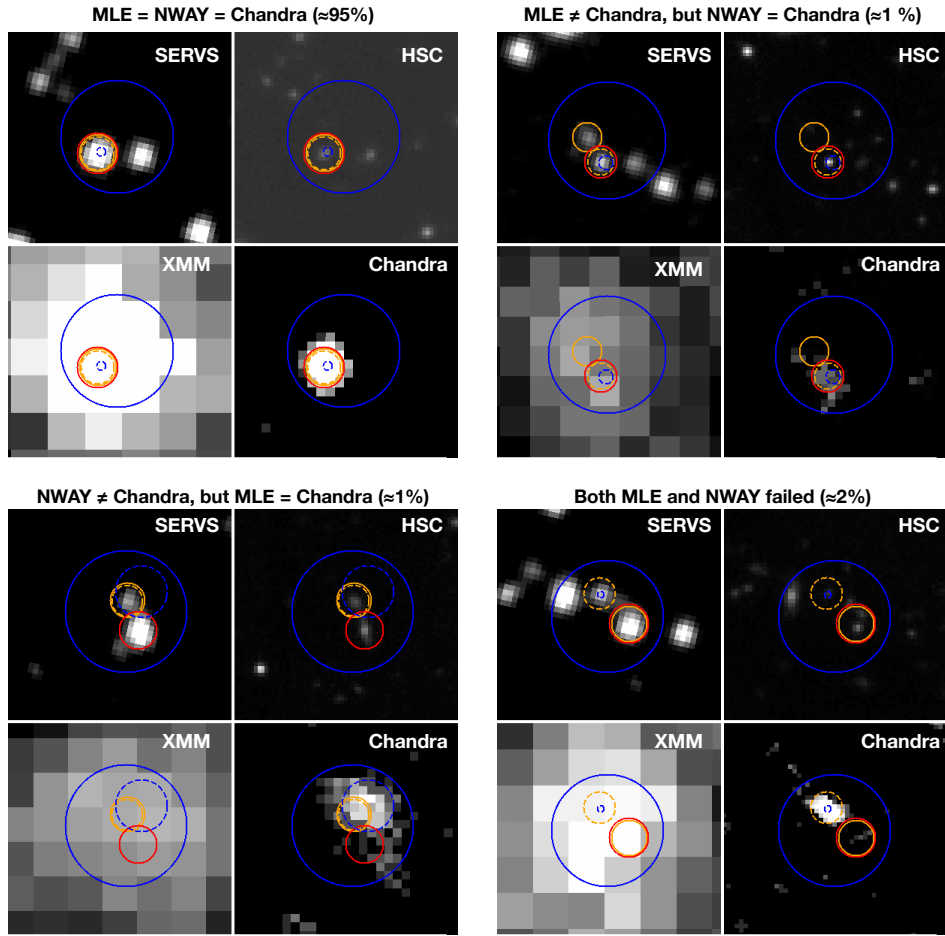


**Figure B1.** Illustrations of the comparison between the matching results using *XMM-Newton* positions or *Chandra* positions for four X-ray sources in our sample. Within the panel for each source, we show images from SERVS [3.6 $\mu$ m](top-left), HSC *i*-band (top-right), *XMM-Newton* 0.5–10 keV (bottom-left), and *Chandra* 0.5–7 keV (bottom-right). X-ray positions are marked as blue circles with a 99.73% error radius, with the *XMM-Newton* positions marked using solid lines and the *Chandra* positions marked using dashed lines. SERVS counterparts identified with the *LR* method are marked as orange circles with a 2'' radius, solid lines mark the counterparts of the *XMM-Newton* positions, and dashed lines mark the counterparts of the *Chandra* positions. SERVS counterparts of the *XMM-Newton* positions identified using NWAY are shown as the red circles. For the vast majority of *XMM-Newton* sources with *Chandra* counterparts from CSC, our counterpart-matching results are identical to the results obtained using *Chandra* coordinates and positional uncertainties.

higher than 50% of  $p_{-i}$  (Best) are also flagged by NWAY as MATCH\\_FLAG = 2.

Similar to our *LR* approach, we make use of the *Chandra* sources in the XMM-LSS field to compute the priors of the expected counterparts. We use the “auto” functionality of NWAY with a 1.5'' search radius for defining the “real” counterparts. In addition to the magnitude priors, we also include an additional prior based on the *Spitzer* IRAC color from SERVS, [3.6 $\mu$ m]/[4.5 $\mu$ m]. Since the majority of our X-ray sources are expected to be AGNs, the distinct [3.6 $\mu$ m]/[4.5 $\mu$ m] mid-IR color of luminous AGNs will provide additional discerning power. For a small number of sources, this additional prior is useful for discerning two adjacent SERVS sources with comparable magnitudes (see the top-right panel of Fig. B1 for illustration).

After computing the magnitude and IRAC color priors using the *Chandra* sources, we run NWAY on the full X-ray catalog with a search radius of 10''. All four OIR catalogs are

considered simultaneously. We report the multiwavelength matches with MATCH\\_FLAG=1,2 in in Table B supplementary to the *LR* matching results.

Here we also discuss how we estimated the reliability of NWAY matching results. Since NWAY matches all four OIR catalogs simultaneously, we cannot determine the spurious matching rates for the “associated” and “isolated” populations as we did for estimating the spurious matching rates for *LR* results using Monte Carlo simulations (see §5.2). Salvato et al. (2017) suggest that the NWAY matching reliability can be determined by a  $p_{-any}$  threshold, which is chosen based on re-running NWAY on randomly shifted “fake” X-ray catalogs. However, this approach is equivalent to estimating the spurious matching rates for the “isolated” population using the Broos et al. (2007) method, which is usually much higher than the results obtained with the two-population approach (see Broos et al. 2007, Xue et al. 2011, and §5.2 for details). Therefore, we do not adopt any  $p_{-any}$

thresholds for the NWAY matching results. The NWAY matching results can still be assessed by investigating the CSC-matched subsample of 223 X-ray sources, and we find that the difference between the matching results obtained using *Chandra* and *XMM-Newton* positions with NWAY are similar to the *LR* results described in §5.2.

We also use the 223 *Chandra*-detected subsample as a baseline for comparing matching results obtained using the NWAY or *LR* methods. We focus only on comparing the SERVS counterparts, as the vast majority of *LR* matching results are decided based on the primary counterparts from SERVS. We confirm that all *Chandra* sources have the same SERVS matching results using *LR* and NWAY. Therefore, we can use the *Chandra* results obtained with *LR* to assess the matching reliability of both *LR* and NWAY matching results with *XMM-Newton* positions. We show examples of such comparisons in Fig. B1. We find that 95% of the sources have the same matching results from *LR*, NWAY, and *Chandra*. A small fraction (two sources) of *LR* matching results do not agree with those of *Chandra* but could be recovered by NWAY. On the other hand, two of the NWAY matching results do not agree with the *Chandra* results but could be identified by *LR*. Five of the *Chandra* sources have different SERVS counterparts than both the *LR* and NWAY results. *Chandra* and OIR images of these sources suggest that they are either two X-ray sources blended in the *XMM* PSF, or there are multiple OIR counterparts with very similar magnitudes and distances to the X-ray position, and thus it is not surprising neither *LR* nor NWAY could successfully recover the correct counterparts. As demonstrated in Fig. B1, these five sources have multiple counterparts with comparable magnitudes and similar spatial separations from the *XMM-Newton* position. This suggests *LR* and NWAY perform similarly for finding SERVS counterparts.

When further scrutinizing the 95% of sources with identical SERVS counterparts from *LR*, NWAY, and *Chandra*, we find that NWAY cannot identify the correct counterparts in the other three OIR catalogs for a small fraction ( $\sim 10\%$ ) of sources. For instance, one of the X-ray sources has a reliable SERVS counterpart identified by both NWAY and *LR*. For the SERVS counterpart, there is only one VIDEO source within the 0.5'' positional error circle of SERVS. For the *LR* approach described in §5.1, the VIDEO source is associated to the correct SERVS counterpart. However, NWAY does not consider this VIDEO source to be among the most-probable combination of counterparts from all four OIR catalogs that were being matched simultaneously. This is likely due to how NWAY computes  $p_{-i}$ . When multiple OIR catalogs are taken into account simultaneously,  $p_{-i}$  represents the relative probability of counterparts from *all* OIR catalogs being the correct match. In this example, the VIDEO counterpart has an unlikely magnitude according to the VIDEO magnitude prior; therefore, including the VIDEO source as a correct match would result in a lower  $p_{-i}$  compared to the case where the VIDEO source is excluded from the matched counterparts. Similar mismatches are also found when comparing the NWAY and *LR* matching results for the full *XMM-Newton* catalog. We note that NWAY do not have this behavior when no magnitude or color priors are used. However, without the inclusion of magnitude and color priors, NWAY can only rely on the distance-based priors, therefore losing the critical discerning powers for match-

ing *XMM-Newton* sources to the dense OIR catalogs. Further corroborating the Bayesian method's effectiveness of counterpart-matching with multiple OIR catalogs is beyond the scope of this work. Therefore, we list the NWAY matching results as-is in Table B, and we consider only the *LR* matching results listed in Table A when exploring the multiwavelength properties of the X-ray sources reported in this work.

The matching results obtained using NWAY are shown in Table B, and the descriptions of its columns are listed below. Only the counterparts with  $\text{MATCH\_FLAG} \geq 1$  are included. Similar to the *LR* matching results, some of the X-ray sources have multiple probable counterparts. In this table, the same X-ray source can have multiple counterparts and the information of each counterpart is given in an independent row. Similar to columns 138–208 of Table A, properties from SERVS, VIDEO, CFHTLS, and HSC-SSP are marked with prefixes “SERVS\_”, “VIDEO\_”, “CFHT\_”, and “HSC\_”, respectively. Null values are marked as –99 throughout the table.

- (1) Column 1: The unique source ID (XID) assigned to the X-ray source.
- (2) Column 2: The posterior probability of the X-ray source to have any correct counterparts,  $p_{\text{any}}$ , for each X-ray source.
- (3) Column 3: The relative probability of a counterpart to be the correct match,  $p_{-i}$ .
- (4) Columns 4–11: RA and DEC of the counterpart in each OIR catalog.
- (5) Column 12–15: The original Object ID of the counterpart from each OIR catalog.
- (6) Columns 16–19: Separation of the X-ray position from the counterpart in each OIR catalog.
- (7) Columns 20–23: SERVS 3'' aperture photometry and the associated uncertainties in the  $3.6\mu\text{m}$  and  $4.5\mu\text{m}$  bands.
- (8) Columns 24–31: VIDEO PSF photometry and uncertainties in AB magnitude in the  $Y$ ,  $J$ ,  $H$ , and  $K_s$  bands.
- (9) Columns 32–41: CFHTLS PSF photometry and uncertainties in AB magnitude in the  $u$ ,  $g$ ,  $r$ ,  $i$ ,  $z$  bands.
- (10) Columns 42–51: HSC cmodel photometry and uncertainties in AB magnitude in the  $g$ ,  $r$ ,  $i$ ,  $z$ ,  $y$  bands.
- (11) Columns 52: Matching flag,  $\text{MATCH\_FLAG}$ . For the most-probable counterparts the flag is set to 1. For other counterparts that are almost as likely as the most-probable counterpart (i.e., with  $p_{-i} \geq p_{\text{any}}$  (Best)), the flag is set to 2.

**Table A.** The main X-ray source catalog with a selection of columns. Empty or null values are marked as -99. The numbers listed on the second row of this table is the column number of the full X-ray catalog with 208 columns. See Appendix A for a detailed description of each column. This table is available in its entirety in machine-readable form online.

XID (1)	RA (2)	DEC (3)	XPOSERR (4)	FB_DET_ML (16)	FB_EXP (19)	FB_BKG (31)	FB_SCTS (43)	FB_FLUX (93)	HR (95)	LX (98)	LR_FLAG.RE (109)	LR_CATALOG (113)	ZBEST (117)	ZSOURCE (178)	CLASS (184)
XMM00000	34.200218	-4.035255	1.44	19.0	59076.2	1.74	83.04	$8.30 \times 10^{-15}$	-99	-99	False	SERVS	-99	-99	3
XMM00001	34.200713	-4.933734	1.45	63.0	61051.8	1.0	82.03	$7.93 \times 10^{-15}$	-99	$8.98 \times 10^{43}$	True	SERVS	1.82	UDSz	2
XMM00002	34.201454	-5.556716	1.96	16.4	29731.6	0.8	29.64	$5.31 \times 10^{-15}$	-99	$2.46 \times 10^{42}$	True	SERVS	0.459	VIPERS	0
XMM00003	34.201466	-4.499315	1.5	23.3	72553.8	1.76	72.37	$5.32 \times 10^{-15}$	-99	$1.37 \times 10^{43}$	True	SERVS	0.959	PRIMUS	2
XMM00004	34.201949	-4.555523	0.93	316.8	87846.9	1.81	351.91	$2.67 \times 10^{-14}$	-0.43	$9.57 \times 10^{42}$	True	SERVS	0.41	SDSS	2
XMM00005	34.202636	-5.690719	1.66	16.5	26430.1	1.01	52.23	$1.30 \times 10^{-14}$	-99	$1.69 \times 10^{44}$	True	CFHTLS	1.932	VIPERS	2
XMM00006	34.203276	-4.315289	1.55	29.2	107957.7	1.79	65.42	$2.94 \times 10^{-15}$	-99	-99	True	SERVS	-99	-99	3
XMM00007	34.203748	-5.433790	1.77	11.3	78270.8	1.54	41.87	$4.71 \times 10^{-15}$	-99	-99	True	VIDEO	-99	-99	3
XMM00008	34.203820	-4.595275	1.17	114.8	83485.0	1.49	168.25	$1.21 \times 10^{-14}$	-0.48	$2.05 \times 10^{42}$	True	VIDEO	0.294	SDSS	3
XMM00009	34.204668	-5.378238	1.35	57.1	93769.9	1.4	101.92	$6.80 \times 10^{-15}$	-99	-99	False	SERVS	-99	-99	3
XMM00010	34.204772	-4.520794	1.51	32.0	77664.5	1.51	71.54	$5.70 \times 10^{-15}$	-99	-99	True	SERVS	-99	-99	3
XMM00011	34.206732	-4.469321	1.25	81.2	63040.8	1.74	132.09	$1.58 \times 10^{-14}$	-99	$2.61 \times 10^{42}$	True	SERVS	0.291	SDSS	0
XMM00012	34.207426	-4.585313	1.54	17.3	94203.8	1.85	67.16	$4.22 \times 10^{-15}$	-99	$6.80 \times 10^{41}$	True	SERVS	0.289	PRIMUS	0
XMM00013	34.208245	-5.295083	1.28	66.6	91655.9	1.22	124.63	$7.18 \times 10^{-15}$	-0.32	-99	True	SERVS	-99	-99	3
XMM00014	34.209443	-4.012790	1.34	34.8	63642.5	1.92	106.5	$9.30 \times 10^{-15}$	-99	-99	True	SERVS	-99	-99	3
XMM00015	34.209479	-4.028269	0.88	349.3	68619.6	1.94	426.86	$4.12 \times 10^{-14}$	-0.12	$1.26 \times 10^{44}$	True	SERVS	1.031	SDSS	1
XMM00016	34.209496	-4.421868	1.48	89.5	23041.3	0.22	76.5	$2.31 \times 10^{-14}$	-99	0.0	True	SERVS	0.0	SDSS	0
XMM00017	34.209799	-4.328703	1.12	84.6	115477.7	2.71	194.51	$1.32 \times 10^{-14}$	-99	$2.17 \times 10^{42}$	True	SERVS	0.291	SDSS	1
XMM00018	34.209992	-4.563673	1.14	187.9	88839.2	1.41	181.45	$1.38 \times 10^{-14}$	-0.25	-99	True	SERVS	-99	-99	3
XMM00019	34.210413	-3.890166	1.53	37.9	44730.1	0.95	68.48	$7.55 \times 10^{-15}$	-99	-99	True	CFHTLS	-99	-99	3
XMM00020	34.210863	-5.410119	1.76	11.6	89369.8	1.53	43.01	$2.63 \times 10^{-15}$	-99	-99	True	SERVS	-99	-99	3
XMM00021	34.211423	-5.194363	1.09	104.2	85216.5	1.93	207.87	$1.36 \times 10^{-14}$	-0.36	$1.58 \times 10^{42}$	True	SERVS	0.249	SDSS	0
XMM00022	34.211535	-3.892733	1.62	-99	-99	-99	-99	-99	-99	-99	False	HSC	-99	-99	3
XMM00023	34.211690	-5.313163	1.44	34.3	96622.2	1.24	83.2	$4.54 \times 10^{-15}$	-99	$4.33 \times 10^{42}$	True	SERVS	0.627	VIPERS	2
XMM00024	34.213193	-4.355747	1.64	11.1	100517.8	2.9	54.4	$4.40 \times 10^{-15}$	-99	-99	True	SERVS	-99	-99	3
XMM00025	34.214208	-5.417995	1.75	10.7	88372.6	1.56	43.75	$5.35 \times 10^{-15}$	-99	-99	True	SERVS	-99	-99	3
XMM00026	34.215117	-4.937388	1.82	13.5	64067.0	1.07	38.16	$5.06 \times 10^{-15}$	-99	-99	True	SERVS	-99	-99	3
XMM00027	34.215205	-4.388650	1.73	16.5	67996.2	2.29	45.43	$3.98 \times 10^{-15}$	-99	$4.70 \times 10^{41}$	True	SERVS	0.251	PRIMUS	0
XMM00028	34.215240	-3.918303	1.62	15.1	33523.0	0.94	56.51	$6.71 \times 10^{-15}$	-99	-99	True	SERVS	-99	-99	3
XMM00029	34.217465	-4.087917	1.48	22.2	82858.6	1.96	75.51	$6.05 \times 10^{-15}$	-99	$7.65 \times 10^{42}$	True	SERVS	0.707	PRIMUS	2
XMM00030	34.217481	-5.601158	1.71	17.5	24629.1	1.0	47.25	$1.06 \times 10^{-14}$	-99	$7.02 \times 10^{43}$	True	VIDEO	1.44	SDSS	1

**Table B.** The NWAY matching results with a selection of columns. Empty or null values are marked as -99. See Appendix B for a detailed description of each column.

XID (1)	PANY (2)	PI (3)	SERVS_ID (12)	SERVS_MAG1 (20)	VIDEO_ID (13)	VIDEO_KSMAG (30)	CFHT_ID (14)	CFHT_IMAG (38)	HSC_ID (15)	HSC_IMAG (46)	MATCH_FLAG (52)
XMM00000	0.99	0.96	172727	20.5	644245983190	21.08	1114_031255	21.93	37484971320960508	22.04	1
XMM00001	0.94	1.0	-99	-99	644245946363	17.51	1123_233188	19.29	37484833882002514	19.22	1
XMM00002	1.0	0.99	174016	17.13	644245975018	17.08	1114_024092	17.85	-99	-99	1
XMM00003	0.99	0.6	172557	19.57	644245974364	19.35	1114_023481	20.58	37485108759912843	20.5	1
XMM00004	0.99	0.97	130124	18.41	644245971200	18.41	1114_021145	19.78	37484833882008818	19.85	1
XMM00005	0.99	0.98	-99	-99	-99	-99	1123_211260	20.41	37484692148084612	20.56	1
XMM00006	0.99	1.0	-99	-99	-99	-99	1123_212886	20.98	37484692148084849	21.09	1
XMM00007	1.0	0.99	159785	19.4	644245968189	20.16	1114_018595	21.27	37485108759911057	21.16	1
XMM00008	0.15	0.37	-99	-99	644245967227	19.97	-99	-99	-99	-99	1
XMM00009	0.94	1.0	-99	-99	644246423098	19.85	1114_015512	20.02	-99	-99	1
XMM00010	0.56	0.67	-99	-99	644245971580	21.66	1114_021242	22.87	37484971320960299	21.79	1

## REFERENCES

- Aihara H., et al., 2017, eprint arXiv:1702.08449
- Bradshaw E. J., et al., 2013, *Monthly Notices of the Royal Astronomical Society*, 433, 194
- Brammer G. B., van Dokkum P. G., Coppi P., 2008, *The Astrophysical Journal, Volume 686, Issue 2, article id. 1503-1513, pp. (2008)..*, 686
- Brandt W. N., Alexander D. M., 2015, *The Astronomy and Astrophysics Review*, 23, 1
- Broos P. S., Feigelson E. D., Townsley L. K., Getman K. V., Wang J., Garmire G. P., Jiang Z., Tsuboi Y., 2007, *The Astrophysical Journal Supplement Series*, 169, 353
- Broos P. S., et al., 2011, *The Astrophysical Journal Supplement, Volume 194, Issue 1, article id. 2, 19 pp. (2011)..*, 194
- Brusa M., et al., 2007, *The Astrophysical Journal Supplement Series*, 172, 353
- Cappelluti N., et al., 2007, *The Astrophysical Journal Supplement Series*, 172, 341
- Cappelluti N., et al., 2009, *Astronomy and Astrophysics*, 497, 635
- Chiappetti L., et al., 2005, *Astronomy & Astrophysics*, 439, 413
- Civano F., et al., 2016, *The Astrophysical Journal*, 819, 62
- Coil A. L., et al., 2010, *The Astrophysical Journal, Volume 741, Issue 1, article id. 8, 15 pp. (2011)..*, 741
- Diehl H. T., et al., 2014, in Peck A. B., Benn C. R., Seaman R. L., eds, Vol. 9149, *Proceedings of the SPIE*, Volume 9149, id. 91490V 15 pp. (2014).. p. 91490V, doi:10.1117/12.2056982, <http://proceedings.spiedigitallibrary.org/proceeding.aspx?doi=10.1117/12.2056982>
- Driver S. P., Robotham A. S. G., 2010, *MNRAS*, 407, 2131
- Evans I. N., et al., 2010, *The Astrophysical Journal Supplement Series*, 189, 37
- Franzen T. M. O., et al., 2015, *Monthly Notices of the Royal Astronomical Society, Volume 453, Issue 4, p.4020-4036*, 453, 4020
- Garilli B., et al., 2014, *Astronomy & Astrophysics*, 562, A23
- Hasinger G., et al., 2007, *ApJS*, 172, 29
- Hudelot P., et al., 2012, *VizieR On-line Data Catalog: II/317. Originally published in: SPIE Conf. 2012*, 2317
- Jarvis M. J., et al., 2012, *Monthly Notices of the Royal Astronomical Society*, 428, 1281
- Jarvis M. J., et al., 2017, preprint, ([arXiv:1709.01901](https://arxiv.org/abs/1709.01901))
- Kelson D. D., et al., 2014, *The Astrophysical Journal*, 783, 110
- Kim M., Wilkes B. J., Kim D., Green P. J., Barkhouse W. A., Lee M. G., Silverman J. D., Tananbaum H. D., 2007, *The Astrophysical Journal*, 659, 29
- Klypin A., Yepes G., Gottlöber S., Prada F., Heß S., 2016, *Monthly Notices of the Royal Astronomical Society*, 457, 4340
- LaMassa S. M., et al., 2016, *The Astrophysical Journal*, 817, 172
- Le Fevre O., et al., 2013, *Astronomy & Astrophysics*, 559, A14
- Liu Z., et al., 2016, *Monthly Notices of the Royal Astronomical Society*, 459, 1602
- Lonsdale C. J., et al., 2003, *The Publications of the Astronomical Society of the Pacific, Volume 115, Issue 810, pp. 897-927, 115, 897*
- Luo B., et al., 2010, *The Astrophysical Journal Supplement Series*, 187, 560
- Luo B., et al., 2017, *The Astrophysical Journal Supplement Series*, 228, 2
- Mauduit J. C., et al., 2012, *Publications of the Astronomical Society of Pacific, Volume 124, Issue 917, pp. 714 (2012)..*, 124, 714
- McLure R. J., et al., 2013, *Monthly Notices of the Royal Astronomical Society*, 428, 1088
- Meneux B., et al., 2009, *Astronomy & Astrophysics*, 505, 463
- Menzel M. L., et al., 2016, *Monthly Notices of the Royal Astronomical Society*, 457, 110
- Momcheva I. G., et al., 2016, *The Astrophysical Journal Supple-*  
ment Series, 225, 27
- Moster B. P., Somerville R. S., Newman J. A., Rix H.-W., 2011, *ApJ*, 731, 113
- Nyland K., et al., 2017, *The Astrophysical Journal Supplement Series*, 230, 9
- Oliver S. J., et al., 2012, *Monthly Notices of the Royal Astronomical Society*, 424, 1614
- Pacaud F., et al., 2006, *Monthly Notices of the Royal Astronomical Society*, 372, 578
- Patel S. G., Kelson D. D., Williams R. J., Mulchaey J. S., Dressler A., McCarthy P. J., Shectman S. A., 2015, *The Astrophysical Journal Letters, Volume 799, Issue 2, article id. L17, 5 pp. (2015)..*, 799
- Pierre M., et al., 2016, *Astronomy & Astrophysics*, 592, A1
- Pineau F.-X., et al., 2017, *Astronomy & Astrophysics*, 597, A89
- Polletta M., et al., 2007, *ApJ*, 663, 81
- Ranalli P., et al., 2013, *Astronomy & Astrophysics*, 555, A42
- Ranalli P., et al., 2015, *Astronomy & Astrophysics*, 577, A121
- Rosen S. R., et al., 2016, *Astronomy & Astrophysics*, 590, A1
- Salvato M., et al., 2017, eprint arXiv:1705.10711
- Skelton R. E., et al., 2014, *The Astrophysical Journal Supplement Series, Volume 214, Issue 2, article id. 24, 49 pp. (2014)..*, 214
- Skibba R. A., et al., 2014, *The Astrophysical Journal*, 784, 128
- Sutherland W., Saunders W., 1992, *Monthly Notices of the Royal Astronomical Society*, 259, 413
- Tonry J. L., et al., 2011, *The Astrophysical Journal, Volume 745, Issue 1, article id. 42, 13 pp. (2012)..*, 745
- Ueda Y., et al., 2008, *The Astrophysical Journal Supplement Series*, 179, 124
- Vaccari M., 2016, Proceedings of "The many facets of extragalactic radio surveys: towards new scientific challenges" (EXTRADSUR2015). 20-23 October 2015. Bologna, Italy. Online at <http://pos.sissa.it/cgi-bin/reader/conf.cgi?confid=267>, id.27
- Vaccari M., et al., 2016, in Proceedings of the 4th Annual Conference on High Energy Astrophysics in Southern Africa (HEASA 2016). January 13th, 2016. South African Astronomical Observatory (SAAO), Cape Town, South Africa. Online at <A href="http://pos.sissa.it/cgi-bin/reader/conf.cgi?confid=275">http://pos.sissa.it/cgi-bin/reader/conf.cgi?confid=275</A>, id.26. p. 26 (arXiv:1704.01495)
- Watson M. G., et al., 2008, *Astronomy and Astrophysics*, 493, 339
- Xue Y. Q., 2017, *New Astron. Rev.*, 79, 59
- Xue Y. Q., et al., 2011, *The Astrophysical Journal Supplement Series*, 195, 10
- Yang G., et al., 2014, *The Astrophysical Journal Supplement Series*, 215, 27
- Yang G., et al., 2016, *The Astrophysical Journal, Volume 831, Issue 2, article id. 145, 20 pp. (2016)..*, 831
- de la Torre S., et al., 2010, *Monthly Notices of the Royal Astronomical Society, Volume 409, Issue 2, pp. 867-872..*, 409, 867

This paper has been typeset from a *TeX/LaTeX* file prepared by the author.